234 (2024) 212673

Contents lists available at ScienceDirect

Geoenergy Science and Engineering

journal homepage: www.sciencedirect.com/journal/geoenergy-science-and-engineering

Origin of quartz and its implications for different phase fluids in lacustrine shales from the Qingshankou Formation, southern Songliao Basin, China

Lei Li [a,b], Zhidong Bao [a,b,*], Zhongcheng Li [c], Li Chen [c], Xiaohong Xu [c], Yilin Li [a,b], Yonggang Zhao [d], Xinmin Song [e]

[a] College of Geosciences,China University of Petroleum-Beijing, Beijing, 102249, China
[b] State Key Laboratory of Petroleum Resource and Prospecting, China University of Petroleum-Beijing, Beijing, 102249, China
[c] Research Institute of Exploration and Development, PetroChina Jilin Oilfield Company, Jilin, 138000, China
[d] Xi'an Shiyou University, 710065, Xi'an, China
[e] PetroChina Research Institute of Petroleum Exploration and Development, Beijing, 100083, China

ARTICLE INFO

Keywords:
Quartz types
Silica origin
Different phase fluids
Lacustrine shale
Songliao basin

ABSTRACT

Quartz, an important mineral that occurs in lacustrine shales, can be of different types and origins. Yet, only few studies have investigated how quartz from different sources contribute to phase fluids, such as adsorbed and free fluids present within shale matrix pores. This study integrates various experimental techniques, including X-ray diffraction analysis, geochemical analysis, scanning electron microscopy, energy-dispersive X-ray spectroscopy, and high-frequency two-dimensional nuclear magnetic resonance analysis to quantitatively characterize the different phase fluids associated with various types of quartz occurring in the Qingshankou Formation shale. The characterization results indicated four distinct quartz types: silt-sized quartz, microcrystalline quartz linked with clay minerals, organism-skeletal quartz, and quartz aggregates comprising multiple crystals. The Fe–Al–Mn ternary diagram and SiO_2 versus Zr scatter plot indicate that terrigenous clastic material is the primary source of SiO_2 in shale quartz. Smectite-to-illite transition plays a pivotal role in authigenic quartz formation. Based on quartz concentration data obtained using major element analysis, we estimated the ranges of terrigenous clastic quartz, diagenetic quartz formed by the smectite-to-illite transition, and biogenic quartz concentrations to be from 55.49% to 92.03% (average 84.70%), 6.67%–20.30% (average 13.12%), and 0%–24.21% (average 2.17%), respectively. The solid organic matter in shale is affected by both terrigenous detrital quartz and authigenic quartz transformed from the clay in the basin. Authigenic quartz, formed by the smectite-to-illite transition, considerably enhances the development of solid organic matter in the Qingshankou Formation. By contrast, an abundance of terrigenous detrital quartz can lead to a dilution of the solid organic matter. Thus, this study provides the first direct evidence that along with a high value of bio-organic matter yield factor, the source of quartz plays a significant role in controlling organic matter abundance.

1. Introduction

As the global energy demand grows, unconventional resources, such as shale oil and gas, are gaining increased attention (Pan and Connell, 2015). The petrophysical properties, pore structures, and fluid behaviors of shale reservoirs are closely related to the mineral composition of their shales (Williams et al., 1985; Peng et al., 2020). Quartz, an important mineral in organic-rich shale, constitutes a substantial portion of the total mineral composition in shale reservoirs, such as the Songliao Basin and Ordos Basin in China and the Barnett Shale in North America (Loucks and Ruppel, 2007; Bai et al., 2022). In-depth studies on quartz types and origins can contribute to the prediction of sweet spots and the effective development of shale reservoirs. As a result, exploration costs could be reduced and resource utilization efficiency could be improved (Bowker, 2003).

Over the past few decades, significant progress has been made in the study of quartz in sedimentology (Loucks and Ruppel, 2007; Milliken et al., 2012, 2013). Some researchers have accurately determined the origins of quartz minerals by examining their stable isotopes, trace elements, fluid inclusions, mineral compositions, and particle

* Corresponding author. College of Geosciences, China University of Petroleum-Beijing, No. 18, Fuxue Road, Changping District, Beijing, 102249, China.
E-mail address: baozhd@cup.edu.cn (Z. Bao).

https://doi.org/10.1016/j.geoen.2024.212673
Received 29 June 2023; Received in revised form 9 January 2024; Accepted 15 January 2024
Available online 20 January 2024

morphologies, which reveal the sediment origins and depositional environments (Cavosie et al., 2005; Garzanti et al., 2008; Peng et al., 2020). Moreover, some other researchers have deepened their understanding of quartz formation causes and conditions through studies on the composition, structure, and growth process of quartz and its interactions with other minerals (Tera and Wasserburg, 1972; Martínez et al., 2019). The development of experimental sedimentology has strongly supported research on the origins of quartz. Approaches such as simulation experiments and numerical modeling allow for the enhanced intuitive observation and analysis of quartz-sediment generation processes, further revealing the physical, chemical, and biological mechanisms behind quartz genesis (Lasemi et al., 1990; Wang et al., 2017). Advances in quartz research within sedimentology have provided valuable insights into shale exploration and development. As technology progresses, research on shale quartz will continue to deepen, providing essential foundations for optimizing shale reservoir prediction, exploration, and development strategies.

Phase fluids in shale are the liquids (water, natural gas, oil, etc.) found within shale pores (Fleury et al., 2013; Blattmann et al., 2019). Factors such as pore structure, porosity, pore connectivity, and geological structure of shale along with shale rock physical properties influence the properties and distribution of phase fluids in shale (Dong et al., 2019; Ge et al., 2020). Therefore, a detailed analysis and evaluation of different phase fluids in shale are necessary during the development of shale reservoirs to understand their characteristics and shale production potential. Researchers have recognized the importance of the use of techniques such as mercury injection, scanning electron microscopy (SEM), and X-ray fluorescence spectroscopy to identify different phase fluids (Josh et al., 2012; Cao et al., 2016; Yang et al., 2018a). However, these techniques, focusing mainly on qualitative identification of phase fluids, cannot accurately determine the concentration of different phase fluids. Two-dimensional nuclear magnetic resonance (2D NMR), a nondestructive experimental method that does not require the preparation of special samples, can effectively identify the different phase fluids (Fleury and Romero-Sarmiento, 2016; Blattmann et al., 2019). By conducting 2D NMR experiments, the fluid components and their distribution in shale can be directly observed, which would help determine the influence of quartz on different phase fluids. Additionally, the application of the 2D NMR technique contributes to gain an enhanced understanding of the physical properties and development potential of shale reservoirs.

Unlike in other shale basins, the formation and enrichment of shale oil in the Qingshankou Formation of the Songliao Basin is closely linked to organic matter (OM) and quartz minerals (Wang et al., 2023). The abundance of OM is a factor that determines whether shale, as a source rock, has the potential to generate substantial amounts of shale oil under appropriate thermal maturity conditions. Moreover, the composition of quartz minerals and the fluidity of oil within shale significantly influence postfracturing reservoir modification, which plays a crucial role in achieving efficient oil production. The state of oil within the shale also greatly influences the methods employed for shale oil extraction (Sun et al., 2021). However, because of the high clay mineral content of the Qingshankou Formation shale, further studies on many theoretical issues have become necessary. The intricacy of quartz in the Qingshankou Formation shale, compounded by the diversity of SiO_2 origins, has obscured the relationship between the quartz minerals and solid OM (including kerogen and solid bitumen) in the shale. Consequently, the occurrence of light hydrocarbon fluids (adsorbed and free states) in the shale has not yet been fully understood. Thus, we attempted to address this knowledge gap by investigating the types and origins of the quartz in the Qingshankou Formation shale of the southern Songliao Basin, China through experimental techniques, such as XRD, geochemical analysis, SEM, and energy-dispersive spectroscopy (EDS). Furthermore, we utilized high-frequency 2D NMR analysis to quantitatively characterize the different phase fluids associated with various quartz types to elucidate the implications of quartz origins for phase fluids. The objectives of this study were to (1) investigate the type and characteristics of the quartz in the Qingshankou Formation shale; (2) collect direct evidence of siliceous origins, identify the origins of different quartz types; and (3) elucidate the implications of quartz origin for different phase fluids.

2. Geological setting

The Upper Cretaceous global climate was generally considered warm and humid (Jenkyns, 2010; Haq, 2014), with high sea levels (MacLeod et al., 2013; Zhang et al., 2022) (Fig. 1a). The Songliao Basin, located in northeastern China, is a large oil and gas basin covering a total area of 26×10^4 km (Zhang et al., 2021). The southern Songliao Basin comprises four primary tectonic units: central depression, southeast uplift, western slope, and southwest uplift (Feng et al., 2010) (Fig. 1b). The study area was located in the central depression of the southern Songliao Basin, encompassing four secondary structural units: Honggang terrace, Fuxin uplift belt, Changling depression, and Huazihijie terrace (Xi et al., 2016).

The significant water influx that occurred during the deposition of the Qingshankou Formation in the Songliao Basin led to the formation of an extensive depression basin characterized by a widespread lake distribution and varying water depths, ranging from shallow to deep lakes (Fig. 2a). This substantial water influx played a crucial role in sedimentary processes, influencing the depositional environment and facilitating organic-rich shale accumulation within the basin (Blattmann et al., 2019). The OM in the Qingshankou Formation shale in the central depression area primarily comprises Type I and II_1 kerogens, with high OM concentrations and a high degree of thermal evolution (Ro values of 0.5%–1.3%, averaging to 1.05%) (Blattmann et al., 2019; Liu et al., 2019b). Controlled by the provenance and depositional environment, multiple regional and stable shale formations have formed in the southern Songliao Basin, ranging from the delta front surfaces of the Daqingzijing Delta to the deep lake surfaces of Songyuan Da'an. These formations have created two types of shale reservoirs (Liu et al., 2021) (Fig. 2b).

3. Samples and methods

3.1. Samples

The shale samples used in the study were collected from two wells in the central depression of the southern Songliao Basin, namely Well A located in inshore shallow lake facies (sampling depth: 2310–2470 m), and Well B located in the deep lake–semi deep lake areas (sampling depth: 2250–2380 m). A total of 47 core samples were collected: 25 from the Qingshankou Formation of Well A and 22 from Well B (locations shown in Fig. 2b). All shale samples were initially subjected to rapid pyrolysis, total organic carbon (TOC) testing, and whole-rock and clay mineral composition analysis. Subsequently, an OM extraction experiment was conducted using a Soxhlet extraction device following the experimental procedure outlined in the SY/T 5118-2005 standard for determining chloroform asphalt in rocks (Bai et al., 2021).

3.2. Methods

Shale samples from Well A and Well B were cut into regular shapes using bridge plugs. To prepare the shale samples for geochemical analysis, a sequential polishing procedure was employed. The process began with mechanical polishing to achieve a smooth surface, followed by highly precise argon ion milling using the state-of-the-art Fischione Model 1060 SEM Mill. This meticulous sample preparation ensured the removal of any surface irregularities, enabling accurate and detailed analysis of the shale samples. Optical microscopy observations were performed using the Leica 4500P high-precision microscope. SEM was performed using the Nova NanoSEM 450 field emission-SEM with a

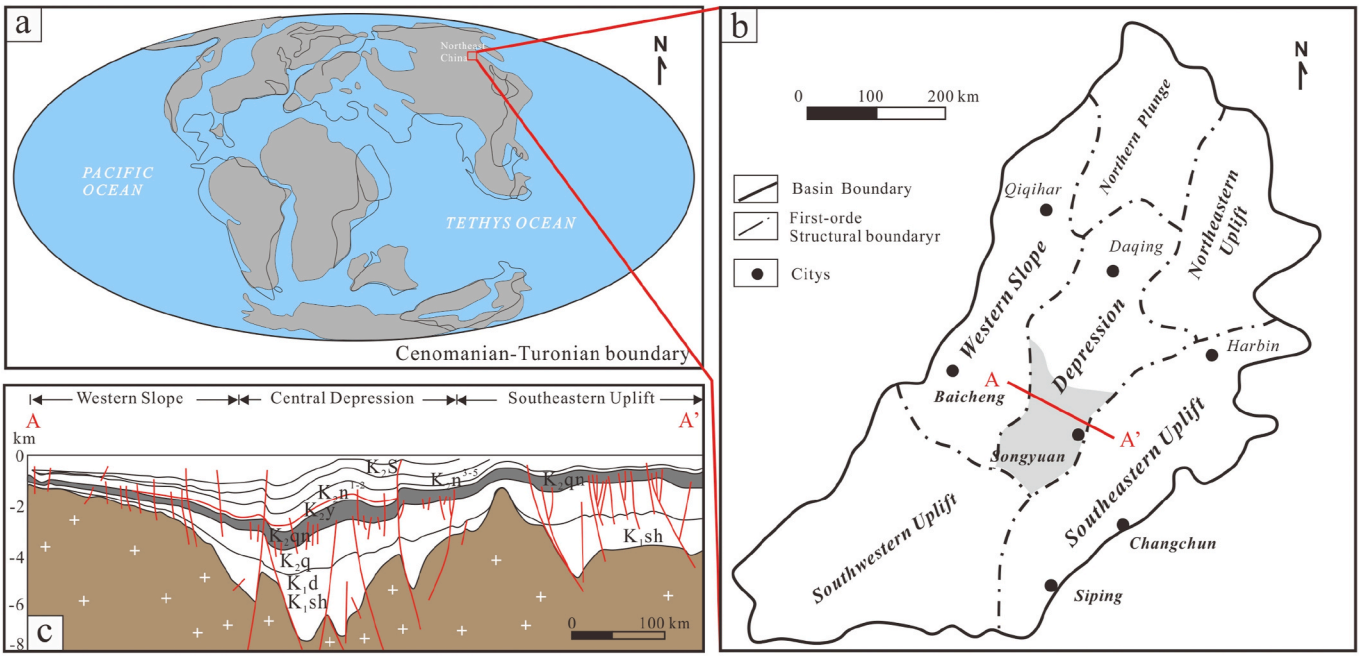

Fig. 1. (a) Global distribution of the Songliao Basin (Zhang et al., 2022). (b) Tectonic map of the Songliao Basin (Feng et al., 2010). (c) Structural cross-section of the Songliao Basin (Feng et al., 2010; Zhang et al., 2022).

built-in Oxford X-Max 80 energy spectrometer and a backscattering probe operating at 15 kV, with a spot size of 5.5 nm and a working distance in the range of 5.0–6.5 mm (Chen et al., 2022).

The samples were pulverized to 200 mesh to avoid contamination and then analyzed. The XRD analysis of the rock and clay mineral concentrations complied with the standard SY/T 5163–2018 (Blattmann et al., 2019; Zhou et al., 2022). Major element analysis of the shale samples was performed using a state-of-the-art X-ray fluorescence spectrometer, which provided accurate elemental compositions. For the trace element analysis, an advanced mass spectrometer was employed, enabling the precise detection and quantification of the trace elements in the shale samples (Niu et al., 2018).

No specific samples were required for the 2D NMR experiments; however, to avoid errors caused by the sample state, the test samples were ground to 0.18 mm and homogenized before taking ~20 g of shale from them for the 2D NMR experiments on shale conducted under ambient conditions. The 2D NMR measurements were performed using the high-precision desktop NMR core analyzer MR Cores-XX manufactured in the United States, following the SYT 6490-2007 standard. Transverse relaxation time (T_2) and longitudinal relaxation time (T_1) were measured (Blattmann et al., 2019). The testing parameters employed in the analysis were carefully optimized to ensure accurate and reliable results. The frequency used for the analysis was set at 23 MHz, ensuring suitable resonance conditions for the shale samples. To ensure the effective capture of components with short relaxation times, the echo spacing time was meticulously set at its lowest possible value of 60 μs. Additionally, measures were taken to enhance the signal-to-noise ratio by increasing the number of scan cycles to 30, with each cycle comprising 16 scans. This comprehensive approach facilitated the acquisition of high-quality NMR data, enabling a thorough investigation of the shale samples. The NMR instrument calibration performed for detecting compounds containing ^1H was followed by a T_2 measurement to determine the total concentration of ^1H-containing compounds in the shale samples. The next step involved T_1–T_2 2D NMR detection, which provided a spectrum that could be used for the quantitative analysis of different compounds (Blattmann et al., 2019; Bai et al., 2021) (Fig. 3).

Magnetic fields and radio frequency pulses are employed in 2D NMR techniques to excite NMR signals. The characteristics of the shale oil in different states can be determined by examining the attenuation and phase change of the signals involved (Fleury and Romero-Sarmiento, 2016). In 2D NMR experiments, T_1–T_2 dimensions are commonly used to analyze the relaxation behavior of immiscible fluids across the time scales, revealing information about their pore structures and fluid composition characteristics (Liu et al., 2021). T_1 and T_2 relaxation times of free and solid (or semisolid) protons are significantly different. The T_1 and T_2 relaxation characteristics of the free protons are similar, while the T_1 relaxation times of solid (or semisolid) protons have a narrower range than their T_2 relaxation times, which are shorter than their T_1 relaxation times (Fleury et al., 2013) (Fig. 3). The T_1–T_2 technique provides relaxation information for different hydrogen nuclei within shale samples. The T_1–T_2 ratio directly reflects the interaction strength between the adsorbate and adsorbent (D'Agostino et al., 2014). By separating and classifying the signals within the different relaxation time intervals, the occurrence characteristics of other shale oil states can be identified (Fig. 3).

4. Results

4.1. Mineral compositions

The results of the XRD analysis of the mineral composition of the 47 shale samples obtained from the Qingshankou Formation revealed three primary types of shale: argillaceous, siliceous, and mixed shale (Fig. 4a). Shale primarily contains clay minerals in the range of 32.0%–69.1% (mean: 52.0%), and the most abundant illite in the range of 65.0%–81.0% (mean: 56.0%). It also contains illite–smectite in the range of 15.0%–56.0% (mean: 36.0%), a mixed-layer clay, and a small amount of chlorite in the range of 2.0%–18.0% (mean: 8.2%) (Fig. 4b). Quartz in the range of 19.1%–45.2% (mean: 28.0%), albite in the range of 7.5%–21.6% (mean: 12.6%), and carbonate minerals were also present in the samples at variable concentrations (range: 0%–25% and mean: 5.4%). Carbonate minerals primarily comprise dolomite and calcite along with small amounts of K-feldspar and pyrite (Table 1). The mineral composition of the marine shales of the Longmaxi Formation in the Sichuan Basin is mainly dominated by quartz and clay minerals, and most of that quartz has originated from biogenic SiO_2 (Wang et al., 2018; Zhang

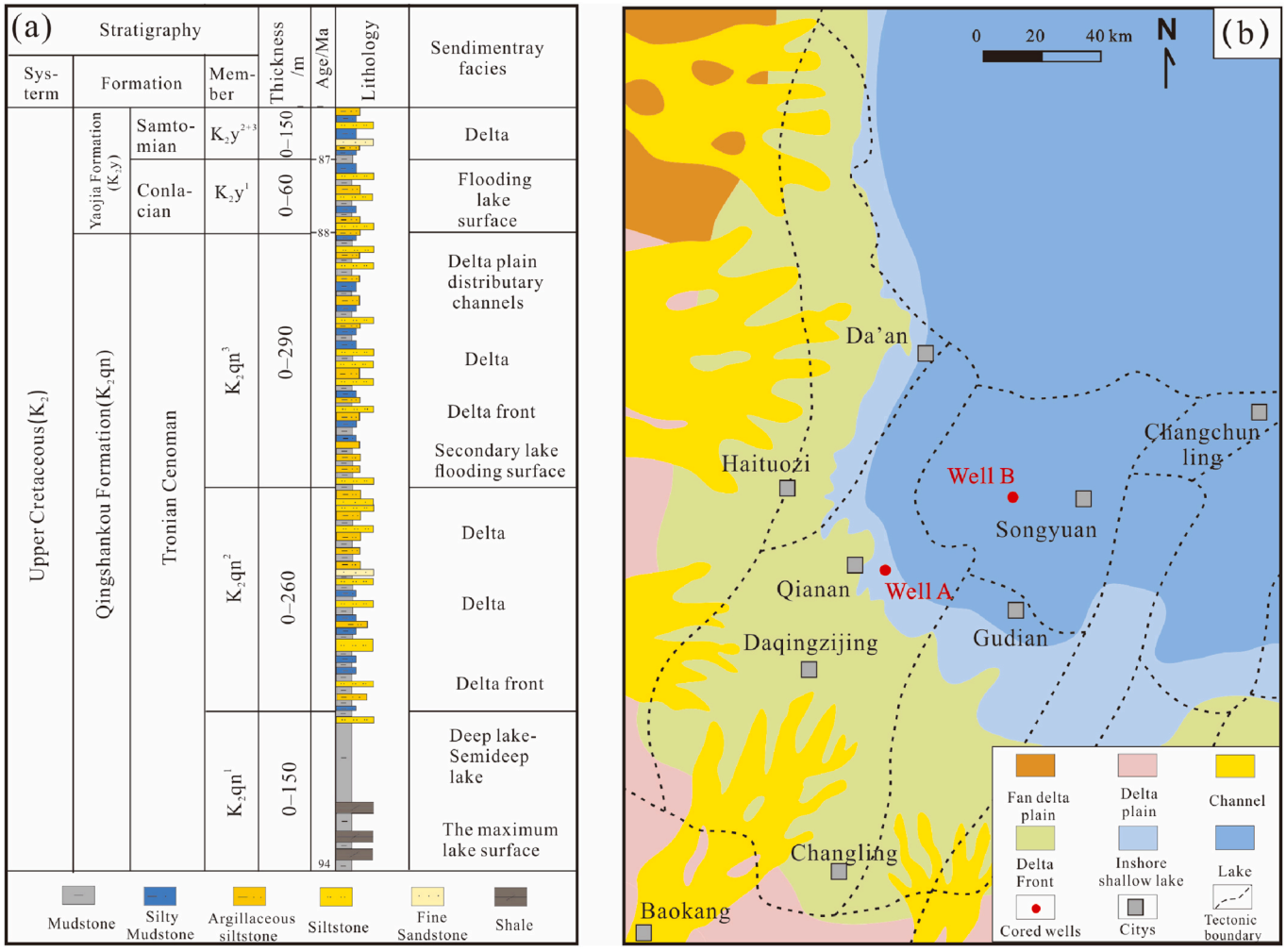

Fig. 2. (a) General lithologic stratigraphy of the Qingshankou Formation (Liu et al., 2019b).(b) Sedimentary facies map (Liu et al., 2021) and locations of Well A and Well B in the central depression of the southern Songliao Basin.

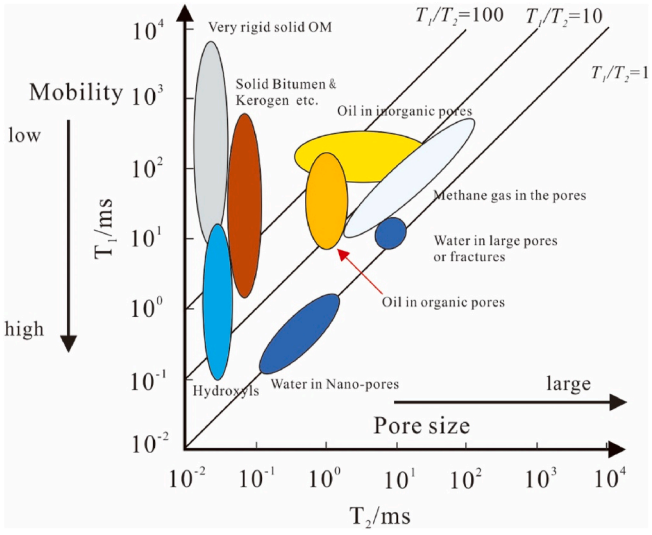

Fig. 3. Signal distribution of different phase fluids and other components in the two-dimensional nuclear magnetic resonance T_1 - T_2 spectrum (Fleury and Romero-Sarmiento, 2016).

et al., 2019). However, the Qingshankou Formation contains a high proportion of shale clay minerals.

4.2. Geochemical analyses

The geochemical characteristics of the 47 shale samples obtained from the Qingshankou Formation are shown in Fig. 5. The figure shows that the TOC concentration of the Qingshankou Formation shale sample ranges from 0.32% to 2.63% with an average of 1.17%. The shale in that sample mainly contained SiO_2 and Al_2O_3 with average concentrations of 56.1% (range: 43.1%–62.2%) and 16.2% (range: 9.2%–18.0%), respectively. The average concentrations of Fe_2O_3 and CaO were 5.4% (range: 3.9%–7.8%) and 3.3% (range: 0.8%–17.8%), respectively. The sample also contained a small amount of MnO, with an average concentration of 0.1% (range: 0.1%–0.2%). The distributions of the major elements vary. The SiO_2 and Al_2O_3 concentrations were higher in Well A, located in the inshore shallow lake, compared with those in Well B, located in the deep lake–semideep lake areas. Moreover, unlike the marine shales (Rezente, 1988), the shale in most of the samples obtained from the Qingshankou Formation contained high amounts of Si.

4.3. Petrographic characteristics of quartz

The quartz contained in shale can be classified into two primary categories: terrigenous clastic quartz and authigenic quartz generated through diagenesis. The characteristics of the terrigenous clastic quartz

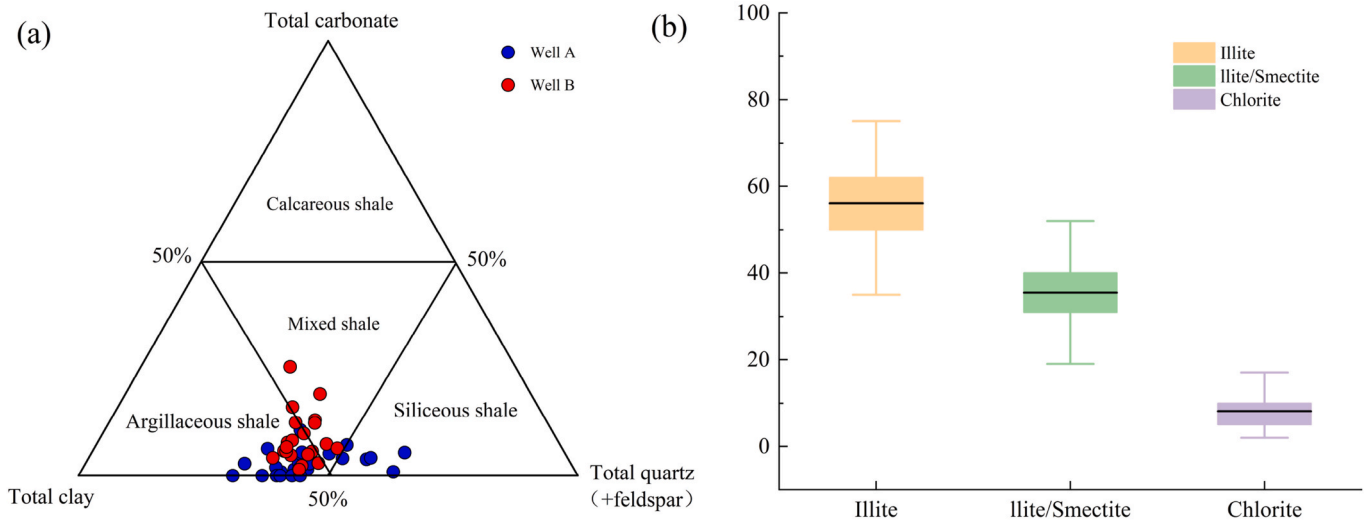

Fig. 4. Classification of shale lithofacies and clay mineral content in the Qingshankou Formation.

can be determined through SEM. The authigenic quartz can be divided into subtypes, which are distinguishable based on the variations in their microscopic structures and adjacent mineral compositions. These classifications align with the results of a previous EDS analysis (Peng et al., 2020; Ye et al., 2022; Yu et al., 2022). Hence, SEM and EDS have elucidated the characteristics and types of quartz present in the Qingshankou Formation shale.

Type I quartz contains silt-sized grains, observable under a microscope. The grains are mostly subrounded and subangular detrital grains (Fig. 6a, b and c), with particle sizes ranging from 5 to 20 μm. The surface traces due to transportation are visible (Fig. 6a). The EDS image shows a pure SiO_2 component in the shale (Fig. 6d and f).

Type II quartz is identified as microcrystalline quartz that coexists with clay minerals in the Qingshankou Formation shale (Fig. 7a). The grains of microcrystalline quartz, typically a few microns in size, appear as dispersed spherical particles or short chain-like or clustered aggregates within or surrounding the clay matrix (Fig. 7b, c, and e). The EDS image shows small amounts of Al and K, implying their possible relationship with clay minerals (Fig. 7d and f).

Type III quartz consists of siliceous skeletal fragments (brown–yellow arrows) appearing as microcrystals (1–3 μm) or aggregates having the same size as fine crystals (10–20 μm) (Fig. 8a). This type of quartz is often embedded in the edges and cavities of biogenic shells in interbedded shales (limestone) (Fig. 8a) and is highly developed in samples with high silica contents. The composition of SiO_2 as revealed by its spectrum is pure (Fig. 8b).

Type IV quartz comprises quartz aggregates formed by multiple quartz crystals (blue arrows). These aggregates have spotted or vein-like distributions of siliceous materials as observed using polarized light microscopy but their concentrations are low (Fig. 8c). The EDS image shows a pure SiO_2 component (Fig. 8d).

4.4. Results of 2D NMR spectroscopy

Fig. 9 shows four regions identified from Fig. 3 (Fleury et al., 2013; Blattmann et al., 2019; Bai et al., 2021). Region (①) represents the signal area of solid OM, which includes kerogen, solid bitumen, heavy oil, and other high-viscosity hydrocarbon compounds having poor flowability. Owing to the limited resolution of 2D NMR, accurate differentiation of these components is challenging, and thus all the components were classified as solid compounds. The specific compositions of these components make them the main contributors to the TOCs of the shale samples. Region (②) represents the signal area of light hydrocarbons, while Region (③) represents the soluble OM on the surface of a shale matrix, such as clay. Region (④) denotes the water present on the surface of the clay minerals or the adsorbed water in shale pores. In some samples, partial overlapping of Regions (③), (④), and (①) could occur owing to the contribution of substances represented by Regions (④) and (①) to the hydroxyl signal in Region (③). Table 2 presents the absolute quantities of different phase compounds obtained by multiplying the total amount of ^{1}H-containing compounds measured by T_2 NMR, by the percentage of each signal contribution to the total signal during each interval.

The T_2 values in Region (②) of the Qingshankou Formation shale, where the hydrocarbon compounds are located, are different from the T_2 values of marine shales and generally exceed 0.1 ms, (Langford and Blanc-Valleron, 1990). This difference is due to the high concentration of magnetic minerals in continental shale, resulting in low T_2 values. The Qingshankou Formation contains pyrrhotite and other iron-bearing minerals (Table 1), such as pyrrhotite, which decrease the T_2 relaxation time.

5. Discussion

5.1. Quartz source

The origin/formation of quartz, particularly authigenic quartz, in shale has been a challenge for geologists. Despite the different perspectives expressed on the origins of quartz, the sources of quartz can be classified into seven categories: terrigenous clastic deposits (Worden and Morad, 2000; Xiong et al., 2022), hydrothermal deposits (Niu et al., 2018; Sakuma et al., 2022), biogenic silica transformation (Peng et al., 2020; Xu et al., 2021; Ye et al., 2022), clay mineral transformation (Worden and Morad, 2000; Peng et al., 2020; Dong et al., 2021), pressure dissolution of detrital quartz (Chen et al., 2022), volcanic glass or ash transformation (Niu et al., 2018), and feldspar alteration (Yang et al., 2018b; Gao et al., 2022). Based on petrological and geochemical data collected from comprehensive experimental studies, we investigated quartz genesis in the Qingshankou Formation shale and collected direct evidence on the siliceous source, enabling us to differentiate the origins of different quartz types.

5.1.1. Terrigenous clastic quartz

The SEM and EDS images of the shale samples obtained from the Qingshankou Formation revealed that most quartz particles in the samples had diameters ranging from silt to fine sand, with high concentrations of Si and O (Fig. 6). Terrigenous clastic quartz is the most dominant type of quartz in the Qingshankou Formation shale. The

Table 1
Shale mineral composition in the Qingshankou Formation.

Sample ID	Well	Depth (m)	Lithofacies	Mineral composition (wt. %)							Clays relative content (%)		
				Quartz	K-feldspar	Albite	Calcite	Dolomite	Pyrite	Clay minerals	Mixed-layer illite-smectite	Illite	Chlorite
1	Well A	2318.4	Siliceous shale	33.1	3.6	14.2	4.0	/	/	27.3	35	56	9
2	Well A	2343.0	Argillaceous shale	23.1	1.6	14.5	3.2	7.3	6.1	28.1	50	41	9
3	Well A	2353.2	Argillaceous shale	27.4	1.7	13.4	1.4	/	3.6	37.4	59	34	7
4	Well A	2363.0	Argillaceous shale	29.3	1.1	12.2	3.0	/	4.8	36.3	53	36	11
5	Well A	2400.5	Argillaceous shale	30.3	1.8	13.0	1.5	/	3.9	34.7	39	55	6
6	Well A	2401.8	Argillaceous shale	28.8	1.8	9.5	0.9	/	/	47.7	52	44	4
7	Well A	2406.8	Argillaceous shale	26.8	2.5	9.3	/	/	1.9	47.7	61	35	4
8	Well A	2407.1	Siliceous shale	44.9	2.3	15.4	/	/	0.9	18.8	55	35	10
9	Well A	2408.2	Argillaceous shale	21.6	2.0	8.3	/	/	2.8	55.0	58	38	4
10	Well A	2412.4	Argillaceous shale	26.4	2.5	14.5	/	/	1.3	38.3	55	37	8
11	Well A	2414.8	Argillaceous shale	29.7	2.5	9.9	3.7	/	1.3	40.5	53	42	5
12	Well A	2416.7	Argillaceous shale	25.6	2.7	11.4	/	/	/	46.2	59	37	4
13	Well A	2419.5	Argillaceous shale	24.7	1.8	10.3	/	/	/	51.1	46	46	8
14	Well A	2432.1	Argillaceous shale	25.7	2.1	12.6	/	/	/	37.2	62	31	7
15	Well A	2436.0	Mixed shale	29.6	2.5	15.6	2.3	/	2.8	29.1	57	36	7
16	Well A	2437.5	Mixed shale	37.5	0.9	11.8	4.2	/	2.9	30.0	52	36	12
17	Well A	2438.6	Argillaceous shale	29.7	2.3	10.1	5.4	/	/	40.1	52	37	11
18	Well A	2442.5	Argillaceous shale	20.7	1.0	9.2	/	/	/	58.9	48	44	8
19	Well A	2446.5	Argillaceous shale	28.2	2.0	12.6	/	/	/	42.0	52	40	8
20	Well A	2453.5	Siliceous shale	45.1	5.4	12.2	5.3	/	/	14.4	55	33	12
21	Well A	2453.9	Argillaceous shale	22.5	4.8	7.5	6.2	/	/	46.7	59	37	4
22	Well A	2456.0	Argillaceous shale	31.8	2.0	10.6	/	/	/	43.0	63	30	7
23	Well A	2462.1	Siliceous shale	45.2	1.7	8.9	1.8	/	2.0	29.8	50	33	17
24	Well A	2464.3	Siliceous shale	38.4	2.2	15.9	2.8	/	1.3	21.3	52	31	17
25	Well A	2465.2	Argillaceous shale	31.4	2.7	10.8	1.8	/	1.0	38.8	56	35	9
26	Well B	2255.1	Argillaceous shale	24.4	1.5	18.1	1.8	3.8	/	50.4	65	29	6
27	Well B	2263.5	Mixed shale	23.0	1.4	21.6	2.5	4.8	/	46.7	39	52	9
28	Well B	2266.5	Argillaceous shale	27.1	1.6	14.8	3.9	1.0	/	51.6	46	45	9
29	Well B	2279.6	Mixed shale	24.7	1.6	14.7	1.3	11.5	/	46.2	46	36	18
30	Well B	2282.8	Argillaceous shale	23.4	1.6	13.1	0.6	7.0	/	54.3	50	42	8
31	Well B	2293.6	Argillaceous shale	26.4	1.6	15.4	0.9	0.7	/	55.0	75	19	6
32	Well B	2305.6	Argillaceous shale	24.0	2.2	17.4	1.5	0.8	/	54.1	81	15	4
33	Well B	2309.8	Argillaceous shale	27.2	2.0	17.4	2.0	0.9	/	50.5	69	24	7
34	Well B	2311.8	Argillaceous shale	24.9	1.5	12.4	6.7	1.4	/	53.1	62	28	10
35	Well B	2318.3	Argillaceous shale	24.3	1.8	14.1	0.6	4.1	/	55.1	50	35	15
36	Well B	2320.8	Mixed shale	21.9	1.3	11.8	0.7	15.1	/	49.2	56	36	8

(*continued on next page*)

Table 1 (*continued*)

Sample ID	Well	Depth (m)	Lithofacies	Mineral composition (wt. %)							Clays relative content (%)		
				Quartz	K-feldspar	Albite	Calcite	Dolomite	Pyrite	Clay minerals	Mixed-layer illite-smectite	Illite	Chlorite
37	Well B	2326.8	Mixed shale	27.9	1.8	19.0	1.1	5.2	/	45.0	20	24	56
38	Well B	2330.0	Argillaceous shale	24.6	1.6	12.1	1.8	3.9	/	56.0	51	37	12
39	Well B	2331.9	Argillaceous shale	27.0	1.5	10.3	1.4	4.2	/	55.6	46	36	18
40	Well B	2337.1	Argillaceous shale	28.3	1.6	13.6	0.8	0.6	/	55.1	66	28	6
41	Well B	2347.6	Mixed shale	19.1	1.5	9.3	11.3	13.7	/	45.1	61	31	8
42	Well B	2355.5	Mixed shale	26.5	1.5	13.3	2.0	10.1	/	46.6	58	33	9
43	Well B	2357.3	Argillaceous shale	25.5	1.6	11.3	4.0	2.6	/	55.0	67	30	3
44	Well B	2362.6	Argillaceous shale	24.5	1.2	11.2	3.1	1.0	/	59.0	69	28	3
45	Well B	2367.0	Argillaceous shale	27.6	1.2	11.5	9.2	0.5	/	50.0	65	32	3
46	Well B	2369.1	Mixed shale	27.0	1.0	9.4	11.7	0.5	/	50.4	62	36	2
47	Well B	2372.5	Mixed shale	30.5	0.7	7.8	14.4	4.4	/	42.2	63	35	2

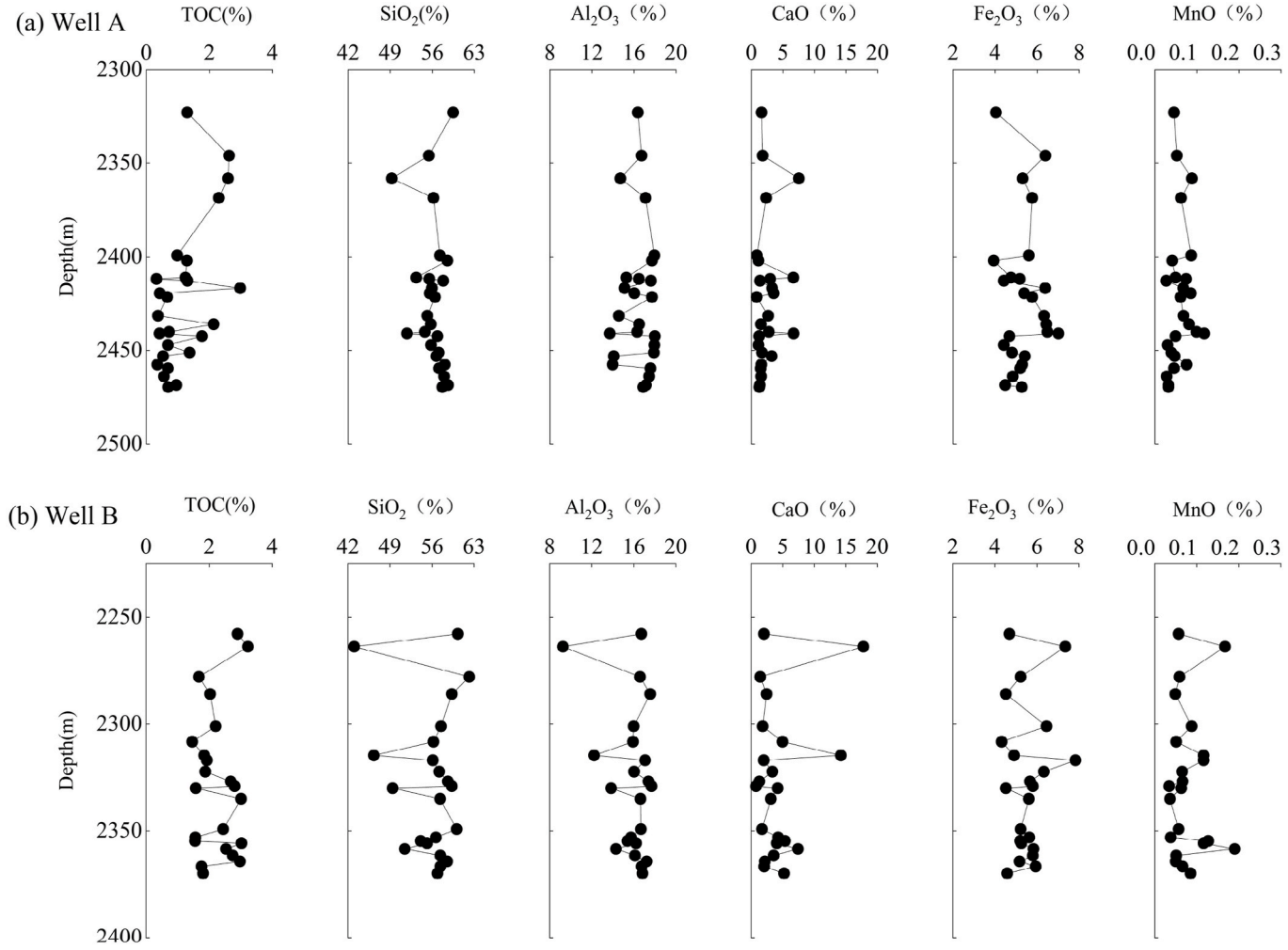

Fig. 5. Distribution of the total organic carbon and major elements in the Qingshankou Formation.

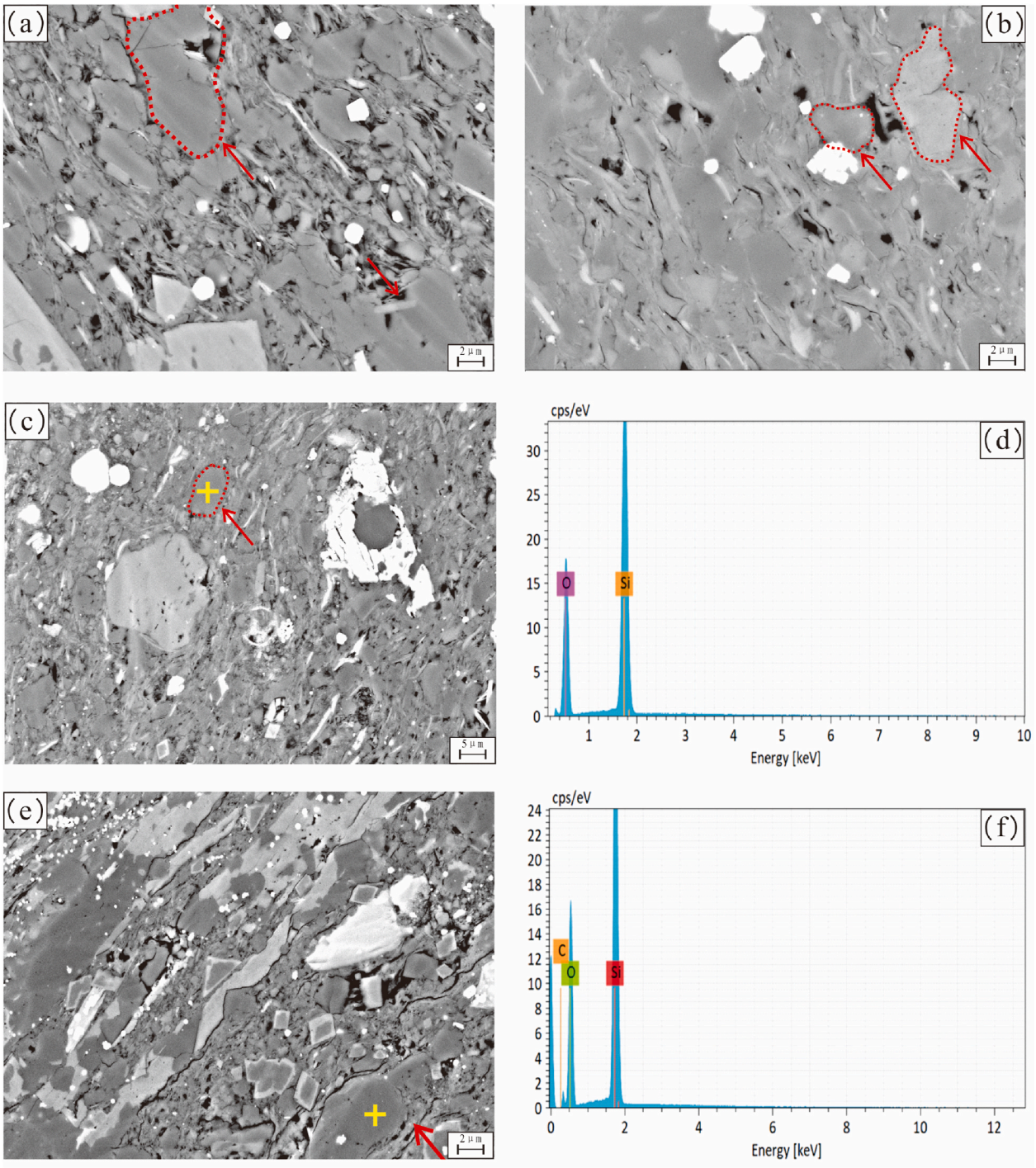

Fig. 6. Scanning electron microscopy (SEM) and energy-dispersive spectroscopy (EDS) images of silt-sized quartz grains (red arrows): (a) and (b) SEM images of detrital quartz silt (red arrows) with subrounded particles; (c) and (e) SEM images showing angular to subangular detrital quartz (red arrows); (d) EDS image of the silt-sized quartz grains marked by the yellow cross in Fig, 6(c); (f) EDS image of the silt-sized quartz grains marked by the yellow cross in Fig. 6(e).

Al–Fe–Mn ternary diagram is commonly used to characterize the formation environment of pyrite (Adachi et al., 1986). We analyzed the Al, Fe, and Mn contents in the shale samples obtained from the Qingshankou Formation, which confirmed the non-hydrothermal origin of the shale. Thus, the source of the Qingshankou Formation quartz in the study area could not have been a hydrothermal silicon source (Fig. 10a).

Trace element analysis showed that SiO_2 and Zr occurring in rocks are related to heavy minerals and that they can therefore be used as indicators of terrigenous clastic input at sand level (Ross and Bustin, 2009). The relationship between SiO_2 and Zr indicates the origin of Si in shale, distinguishing between terrigenous clastic and biogenic sources. A positive correlation between SiO_2 and Zr suggests the predominance of clastic-derived Si in mudstone, while a negative correlation signifies the presence of biogenic quartz (Xi et al., 2019). The correlation we observed between SiO_2 and Zr was positive (Fig. 10b). Siliceous shale displayed a robust positive correlation between SiO_2 and Zr (R^2 = 0.8745), highlighting the substantial influence of terrigenous clasts, primarily on quartz originating from terrigenous sources. Compared

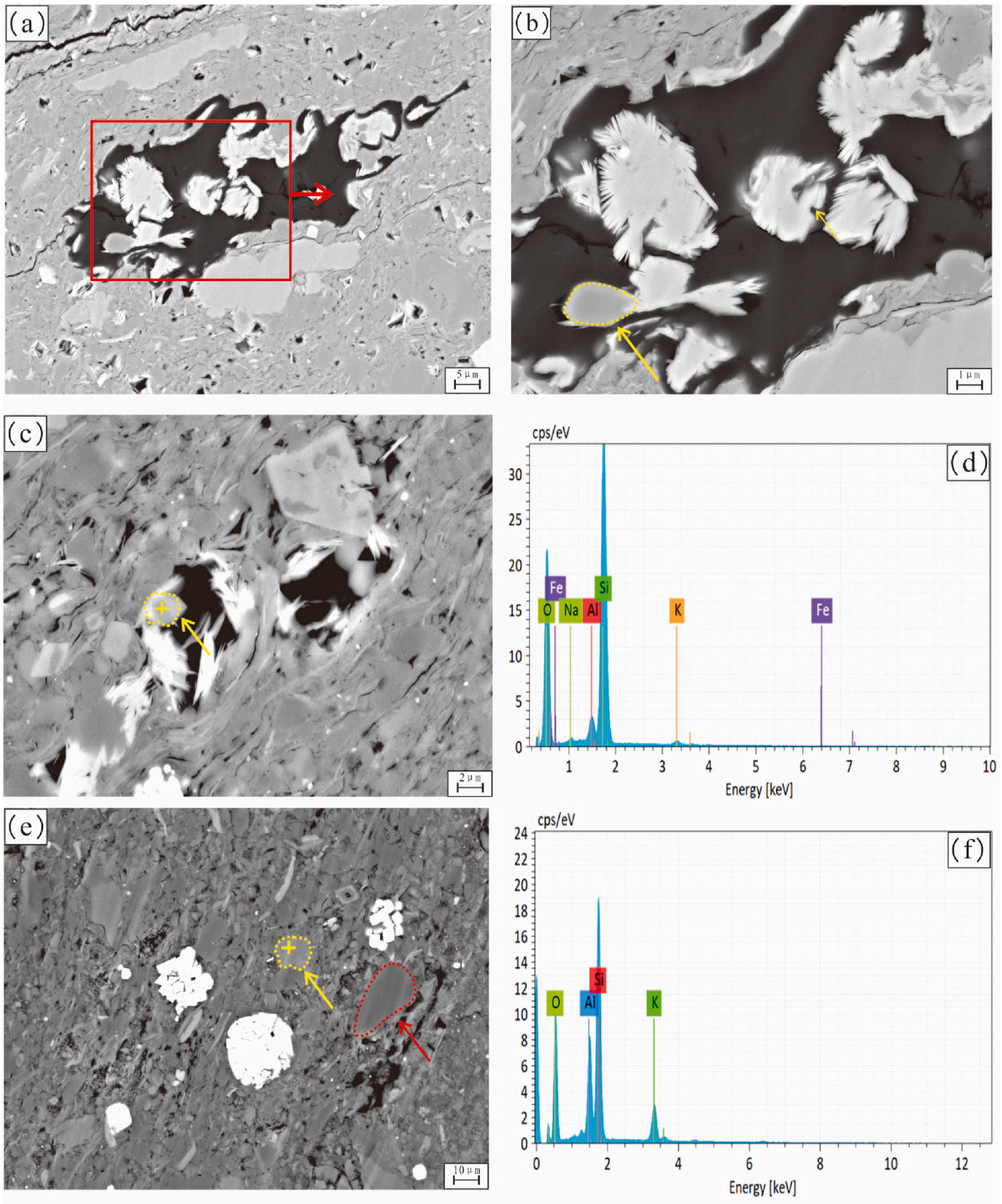

Fig. 7. Scanning electron microscopy (SEM) and energy-dispersive spectroscopy (EDS) images of microcrystalline quartz (yellow arrows) and silt-sized quartz grains (red arrows). (a). SEM images of microcrystalline quartz (yellow arrows) dispersed in organic matter; (b). Area within the red box in (a); (c). SEM images of microcrystalline quartz (yellow arrows) dispersed in the clay matrix; (d) and (f). EDS image of the microcrystalline quartz marked by the yellow cross in (c); (e). SEM image of microcrystalline quartz (yellow arrows) and silt-sized quartz grains (red arrows) showing the microcrystalline quartz surrounded by the clay matrix; (f) EDS image of the microcrystalline quartz marked by the yellow cross in (e).

with siliceous shale, argillaceous shale demonstrated a weaker positive correlation between SiO_2 and Zr ($R^2 = 0.2231$), indicating the lesser impact of terrigenous clasts on quartz of terrigenous origins. Notably, mixed shale exhibited a less evident negative correlation between SiO_2 and Zr, suggesting the existence of biogenic quartz within the samples.

5.1.2. *Smectite-to-illite transition*

Lacustrine shale, rich in clay minerals, is another source of authigenic quartz formed during the transformation of clay minerals. The results of the EDS analysis of the microscale quartz particles of the shale samples obtained from the Qingshankou Formation indicated that the

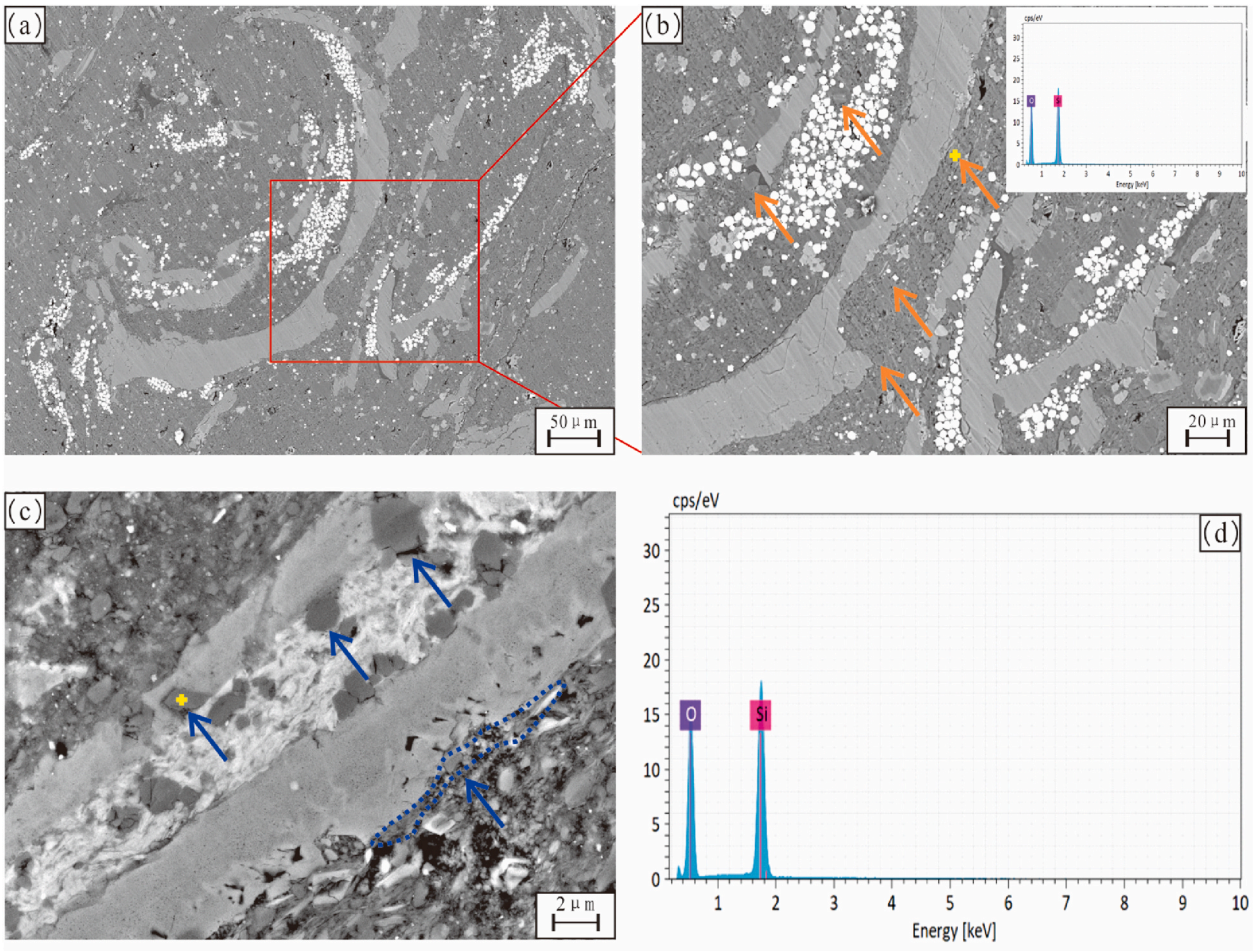

Fig. 8. Scanning electron microscopy (SEM) and energy-dispersive spectroscopy (EDS) images of siliceous skeletal fragments (brown–yellow arrows), and multiple quartz crystals (blue arrows). (a) and (b). SEM images of siliceous skeletal fragments; (c). SEM image of the multiple quartz crystals (green arrows) with vein or point shapes; (d). EDS image of the multiple quartz crystals marked by the yellow cross in (c).

Qingshankou Formation quartz contained Al and K (Fig. 7), indicating that the source of that quartz is related to clay minerals. Additionally, SEM observations revealed a large amount of mixed-layer illite–smectite formed by the replacement of smectite with illite. In some samples, quartz cement crystals were observed to coexist with mixed-layer illite–smectite (Fig. 11b). These petrological characteristics confirm that the smectite-to-illite transition can generate quartz cement crystals.

Previous studies have demonstrated that the smectite-to-illite transition occurs under specific temperature and pressure conditions, mainly at ~80 °C during the middle of the diagenesis phase (Peltonen et al., 2009). During this transition, up to 30% of the mass of smectite is lost, and a large amount of its dissolved SiO_2 is released (Van de Kamp, 2008; Dowey and Taylor, 2017). The released SiO_2 precipitates and crystallizes in situ, forming micron-sized quartz particles. The reaction equation for the smectite-to-illite transition is as follows (Boles and Franks, 1979):

$$K^+ + Smectite \rightarrow Illite + Na^+ + Ca^{2+} + Fe^{2+} + Si^{4+} + OH^- + H_2O \quad (1)$$

According to Equation (1), a sufficient supply of K^+ is necessary for the smectite-to-illite transition to occur. The Qingshankou Formation shale reservoir mainly comprises albite (Table 1), and the dissolution of orthoclase provides some amount of K^+. In addition, the transformation of orthoclase to albite effectively supplies K^+ and promotes the smectite-to-illite transition, generating a large amount of liquid SiO_2 (Bai et al., 2022).

The origin of SiO_2 in clay matrix-dispersed microquartz is primarily attributed to the illitization of smectite, as evidenced by the abundant presence of sheet-like or granular microquartz in proximity to clay minerals. The state of OM within the Qingshankou Formation is characterized as mature, marked by a substantial illitization of smectite, which facilitates the release of SiO_2 and its subsequent precipitation (Metwally and Chesnokov, 2012). XRD data revealed the coexistence of mixed-layer clays and a significant quantity of illite (Table 1), indicating a high degree of illitization. This illitization is a significant contributor to the production of SiO_2, which is crucial for the formation of clay matrix-dispersed microquartz.

5.1.3. Biogenic quartz

The Upper Cretaceous Songliao Basin was characterized by warm and humid paleoclimate (Bechtel et al., 2012). Its sedimentary environment primarily comprised deep to semideep lakes, where abundant bivalves with nodular or rectangular shell shapes thrived, indicating the presence of biogenic SiO_2 (Zhang et al., 2014). The typical major mineral component within the SiO_2-rich biotas was Opal-A, an amorphous and unstable mineral with the molecular formula $SiO_2{\cdot}nH_2O$. During early diagenesis, temperature and pressure caused the buried SiO_2-based biota to dissolve, transforming Opal-A into Opal-CT. This process gradually led to the development of cryptocrystalline and microcrystalline quartz composites with considerable hardness (Dowey and Taylor, 2017; Peng et al., 2020). The size of these quartz particles in the SEM images of the Qingshankou Formation shale aligns with the size of the phosphate nodules and their recrystallization products studied by previous researchers (Xi et al., 2019). However, the Si/(Si + Fe + Al + Ca) ratio of siliceous shale (<0.85) that was observed was between 0.46 and 0.68 (Table 3), (Wedepohl, 1971). This significant discovery further

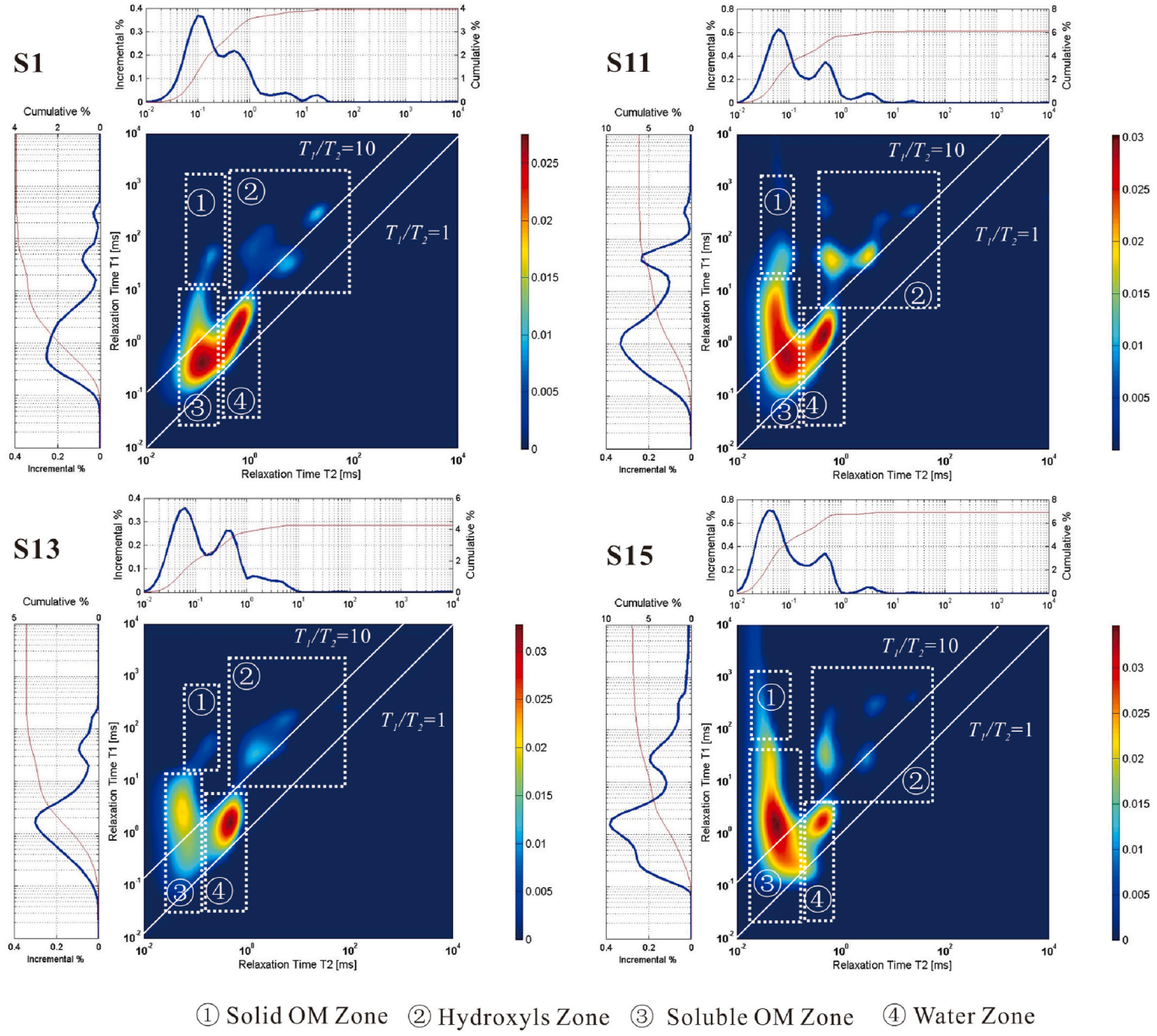

Fig. 9. Two-dimensional nuclear magnetic resonance spectra showing ^{1}H compounds of the shale in the Qingshankou Formation.

confirmed that the biological quartz present in the Qingshankou Formation samples was not primary authigenic quartz.

5.1.4. Feldspar dissolution

During its burial diagenesis, feldspar undergoes dissolution in acidic environments, leading to the formation of kaolinite as an alteration product. However, when K-rich fluids are present, feldspar dissolution can lead to illite precipitation. Sodium feldspar, the dominant mineral in the Qingshankou Formation shale (Table 1), participates in the following reactions:

$$2NaAlSi_3O_8 + 2H^+ + H_2O = Al_2Si_2O_5(OH)_4 + 4SiO_2 + 2Na^+$$

$$3NaAlSi_3O_8 + K^+ + 2H^+ + H_2O = KAl_3Si_3O_{10}(OH)_2 + 6SiO_2 + 3Na^+ + H_2O$$

The acid strength during the diagenetic process of shale can be altered by varying the OM content (Sakuma et al., 2022). The low TOC concentration (average: 1.68%) in the Qingshankou Formation shale (Fig. 5) makes the acidity of the formation weak. Thus, both detrital quartz and feldspar have limited dissolution capacities (Fig. 11c and d), causing a reduction in SiO_2 precipitation followed by a decrease in authigenic silica concentration.

5.2. Percentages of quartz of different origins

From the above-mentioned analysis, we can infer that terrigenous clastic quartz, smectite-to-illite transition, and biogenic quartz are the primary sources of quartz occurring in the Qingshankou Formation shale. Although feldspar dissolution also contributes to the formation of authigenic silica in shale, its influence could be considered negligible (Bai et al., 2022).

Assuming that the Qingshankou Formation shale is within a closed system, the percentages of different types of quartz occurring in the Qingshankou Formation shale were calculated based on the law of mass conservation (Van de Kamp, 2008). Modern shale typically contains more smectite than kaolinite or illite. Thus, the illite in the shale samples was assumed to have been transformed from smectite (Van de Kamp,

Table 2
Bulk fluid contents of the different phases of the shale in the Qingshankou Formation.

Samples	Lithology	Content of all ^1H/μL	Solid OM /(μL·g^{-1})	Hydroxyls /(μL·g^{-1})	Soluble OM /(μL·g^{-1})	Water /(μL·g^{-1})
S1	Siliceous shale	508.090	0.554	1.703	7.639	4.792
S2	Argillaceous shale	673.806	1.750	4.356	17.177	5.955
S3	Argillaceous shale	484.663	2.674	3.106	15.295	5.131
S4	Argillaceous shale	468.461	2.526	4.221	10.563	3.952
S7	Argillaceous shale	619.941	4.014	1.242	11.911	7.348
S8	Siliceous shale	718.853	2.238	2.326	20.498	6.000
S9	Argillaceous shale	818.672	3.678	1.679	16.933	8.888
S11	Argillaceous shale	642.012	2.657	3.337	11.917	4.104
S13	Argillaceous shale	478.752	1.964	3.757	16.278	8.493
S14	Argillaceous shale	726.260	2.649	1.433	15.856	7.055
S15	Mixed shale	711.322	5.651	2.624	14.384	3.943
S20	Siliceous shale	339.717	0.885	1.788	10.233	2.513
S23	Siliceous shale	591.477	2.673	0.671	14.371	3.494
S24	Siliceous shale	566.902	1.495	0.597	13.714	4.250
S27	Mixed shale	229.593	1.645	1.397	5.002	0.764
S28	Argillaceous shale	682.584	2.454	1.867	22.553	4.577
S29	Mixed shale	858.026	3.242	2.001	26.007	7.796
S36	Mixed shale	836.181	4.189	2.327	23.348	9.158
S37	Mixed shale	942.865	3.638	3.195	20.105	6.042
S38	Argillaceous shale	656.531	2.444	3.376	13.567	5.762
S39	Argillaceous shale	721.369	2.061	4.013	15.925	9.099
S41	Mixed shale	769.116	3.571	3.341	21.376	5.246
S42	Mixed shale	568.093	1.957	1.072	13.284	4.302
S43	Argillaceous shale	685.67	3.215	3.527	19.038	5.300
S44	Argillaceous shale	775.247	3.176	1.242	22.528	2.249

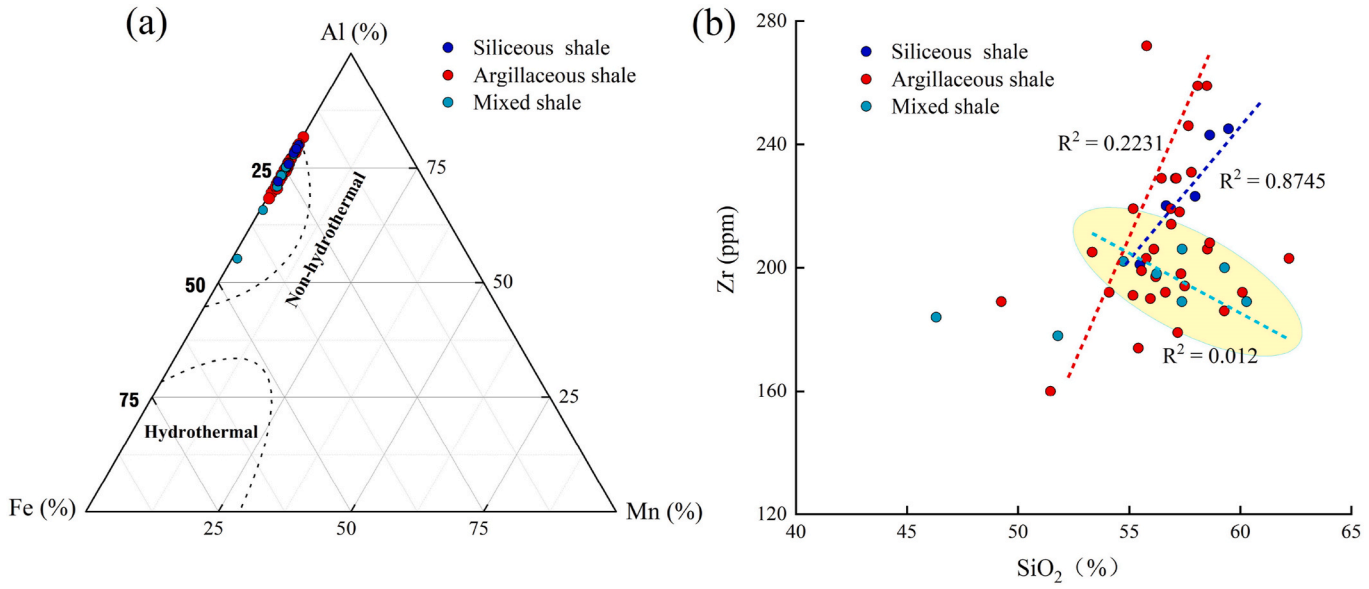

Fig. 10. Discrimination plot for the origin of shale quartz in the Qingshankou Formation.

2008). The smectite-to-illite transition can be written as follows (Van de Kamp, 2008):

$$1.308\{[(Al_{3.15}Mg_{0.85})(Si_{8.0})O_{20}(OH)_4(Na_{0.85})2H_2O][Smectite,1101.1g]+(0.06Fe_2O_3+0.56K_2O+0.02CaO)\}$$
$$\rightarrow[(Al_{4.12}Fe_{0.1}Mg_{0.56})(Si_{7.17})O_{20}(OH)_4(K_{1.47}Na_{0.01}Ca_{0.03})][Iliite,787.2g]+3.29SiO_2[197.7g]+0.56Na_2O+0.55MgO+3.23H_2O$$

The proportions of the three quartz sources in the Qingshankou Formation shale (terrigenous clastic quartz, smectite-to-illite transition, and biogenic quartz) can be calculated using the following equation based on the method presented in Niu et al. (018). The $(Si/Al)_{background}$ is assumed to be the average shale ratio of 3.11 (Wedepohl, 1971).

$$Si_{excess}=Si_{excess}-\left[(Si/Al)_{background}\times Al_{sample}\right]$$

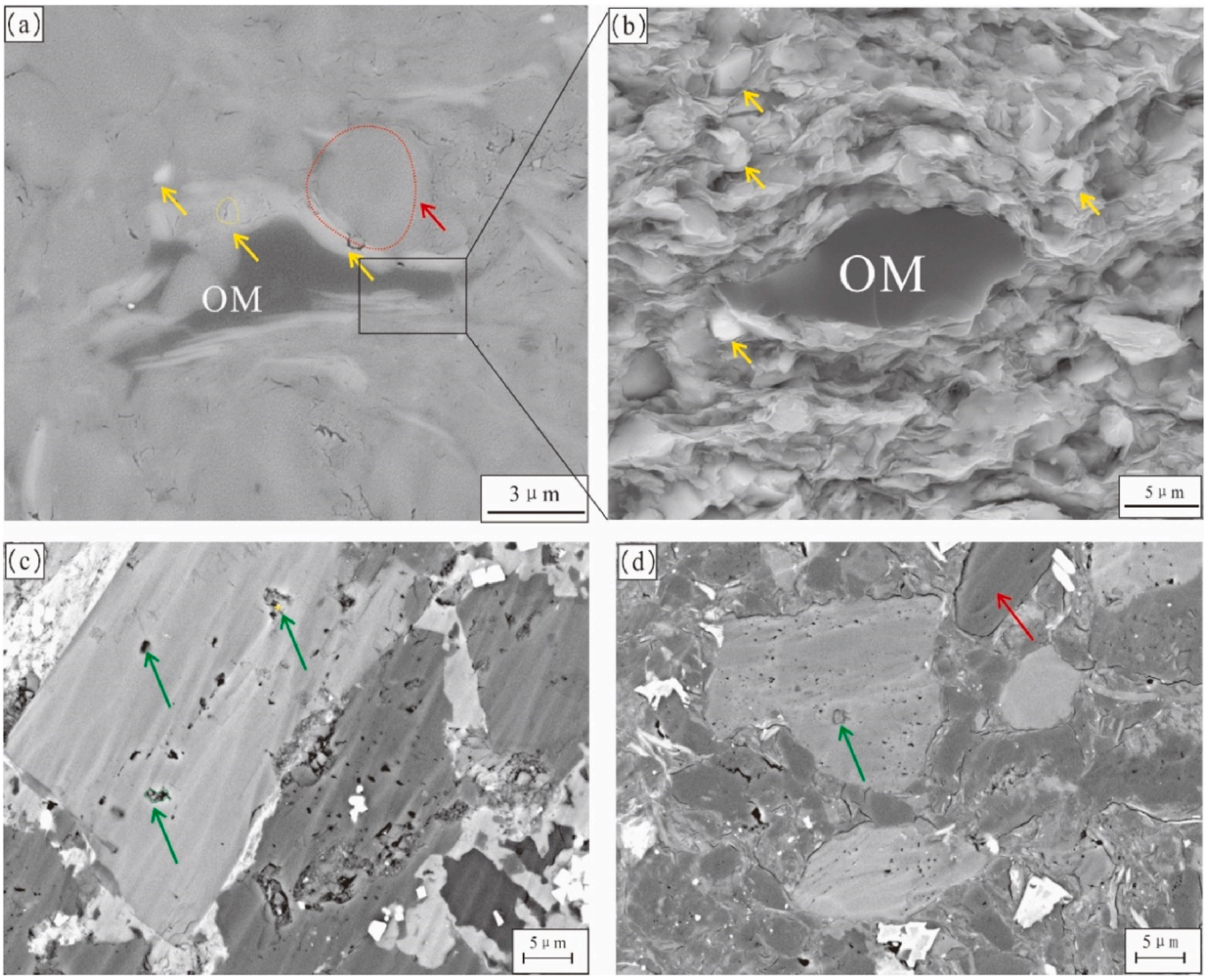

Fig. 11. Scanning electron microscopy (SEM) images of authigenic silica during feldspar dissolution (green arrows) and silt-sized quartz grains (red arrows). (a) and (b). SEM images of quartz cement crystals coexisting with mixed-layer illite–smectite. (c) SEM images of secondary quartz formed by the dissolution of clastic feldspar. (d) SEM images of secondary quartz and unaltered residual plagioclase.

$$SiO_{2\ XX} = (Si/Al)_{XX} / (Si/Al)_{total}$$

$$Si_{2terrigenous} = 1 - Si_{2biogenic} biogenic - SiO_{2\ S-I}$$

where xx corresponds to terrigenous clastic quartz, smectite-to-illite transition, or biogenic quartz, as appropriate. $SiO_{2\ S-I}$ is the SiO_2 sourced from smectite-to-illite transition.

The study results provide significant insights into the mineral composition of the shale in the Qingshankou Formation. Our analysis revealed varying concentrations of terrigenous clastic quartz, diagenetic quartz formed by the smectite-to-illite transition, and biogenic quartz in the shale samples examined (Fig. 12). The data demonstrate that the concentration of terrigenous clastic quartz varies between 92.03% and 55.49%, with an average concentration of ~84.70% (Table 3). This terrigenous clastic quartz component is likely to have originated owing to the introduction of quartz-rich terrestrial material during the sedimentary process. Another significant component is the diagenetic quartz formed by the smectite-to-illite transition, which had concentrations ranging from 20.30% to 6.67% across the samples and an average concentration of ~13.12% (Table 3). Diagenetic quartz is associated with the transformation of clay minerals into quartz during diagenesis, particularly as burial depth and temperature increase. The presence of biogenic quartz with concentrations ranging from 0% to 24.21% across the samples and an average concentration of ~2.1% is noteworthy (Table 3). This component represents quartz originating from biogenic sources, such as the remnants of microorganisms or other biological materials.

Compared with siliceous shale, argillaceous shale contains a higher content of diagenetic quartz formed by the smectite-to-illite transition, while its terrestrial detrital quartz content is slightly lower. This disparity could be intricately linked to the distinct lithological and sedimentary environments within which these two shale types form. Lacustrine argillaceous shale takes shape in sedimentary environments that are distant from the shale source, where sedimentary waters are deep and the influence of terrestrial detritus is low. Thus, it tends to exhibit a high concentration of authigenic quartz.

5.3. *Influence of the quartz origin on phase fluids*

Quartz originating from different sources in shale, such as terrigenous or authigenic quartz, are of different types, while their quantities and spatial distributions are also different, affecting physical properties

Table 3
Major elements, elemental ratios, and calculated percentages of quartz of different origins in the Qingshankou Formation shale.

Sample name	Lithofacies	Major oxides (%)					Excess-Si	Si/(Si + Fe + Al + Ca)	(Si/Al)$_{total}$	(Si/Al)$_{S-I}$	(Si/Al)$_{Biogenic}$	SiO_2 illitization	SiO_2 biogenic	SiO_2 terrestrial
		Fe_2O_3	MnO	CaO	SiO_2	Al_2O_3								
1	Siliceous shale	4.04	0.05	1.61	59.47	16.37	0.94	0.69	3.21	0.21	0.10	6.67%	3.07%	90.26%
2	Argillaceous shale	6.39	0.05	1.78	55.41	16.71	0.00	0.64	2.93	0.33	0.00	11.40%	0.00%	88.60%
3	Argillaceous shale	5.31	0.09	7.52	49.25	14.71	0.00	0.58	2.96	0.41	0.00	14.02%	0.00%	85.98%
4	Argillaceous shale	5.76	0.06	2.33	56.19	17.11	0.00	0.64	2.90	0.37	0.00	12.89%	0.00%	87.11%
5	Argillaceous shale	5.60	0.09	0.89	57.27	17.94	0.00	0.66	2.82	0.39	0.00	13.82%	0.00%	86.18%
6	Argillaceous shale	3.93	0.04	1.11	58.50	17.71	0.00	0.68	2.92	0.38	0.00	13.17%	0.00%	86.83%
7	Argillaceous shale	4.76	0.05	6.67	53.34	15.28	0.00	0.61	3.08	0.53	0.00	17.09%	0.00%	82.91%
8	Siliceous shale	5.17	0.07	2.99	55.49	16.48	0.00	0.64	2.97	0.27	0.00	9.09%	0.00%	90.91%
9	Argillaceous shale	4.42	0.03	1.36	57.80	17.60	0.00	0.67	2.90	0.48	0.00	16.46%	0.00%	83.54%
10	Argillaceous shale	6.38	0.07	3.28	55.95	15.09	1.39	0.64	3.27	0.44	0.16	13.53%	0.23%	86.24%
11	Argillaceous shale	5.39	0.09	3.53	55.56	16.03	0.00	0.64	3.06	0.39	0.00	12.67%	0.00%	87.33%
12	Argillaceous shale	5.76	0.06	0.85	56.46	17.71	0.00	0.65	2.82	0.45	0.00	15.83%	0.00%	84.17%
13	Argillaceous shale	6.33	0.07	2.65	55.17	14.57	1.89	0.65	3.35	0.41	0.24	12.34%	0.00%	87.66%
14	Argillaceous shale	6.44	0.08	1.49	55.77	16.49	0.00	0.65	2.99	0.50	0.00	16.64%	0.00%	83.36%
15	Mixed shale	6.49	0.10	2.76	54.75	16.30	0.00	0.63	2.97	0.39	0.00	13.23%	7.04%	79.72%
16	Mixed shale	7.02	0.12	6.69	51.79	13.69	1.74	0.59	3.34	0.36	0.23	10.77%	6.91%	82.32%
17	Argillaceous shale	4.68	0.05	1.22	56.87	17.98	0.00	0.66	2.79	0.34	0.00	12.06%	0.00%	87.94%
18	Argillaceous shale	4.42	0.03	1.12	55.79	17.94	0.00	0.66	2.75	0.41	0.00	14.93%	0.00%	85.07%
19	Argillaceous shale	4.81	0.04	1.70	57.08	17.90	0.00	0.66	2.82	0.37	0.00	13.09%	0.00%	86.91%
20	Siliceous shale	5.41	0.05	3.23	56.67	14.07	3.41	0.66	3.56	0.28	0.45	7.97%	0.00%	92.03%
21	Argillaceous shale	5.29	0.08	1.57	58.08	13.97	4.23	0.69	3.67	0.46	0.56	12.58%	0.00%	87.42%
22	Argillaceous shale	5.20	0.05	1.48	57.12	17.56	0.00	0.66	2.87	0.44	0.00	15.40%	0.00%	84.60%
23	Siliceous shale	4.83	0.03	1.54	57.97	17.43	0.00	0.66	2.94	0.26	0.00	8.75%	0.00%	91.25%
24	Siliceous shale	4.48	0.03	1.32	58.62	17.14	0.00	0.68	3.02	0.27	0.00	8.78%	0.00%	91.22%
25	Argillaceous shale	5.26	0.03	1.28	57.67	16.88	0.00	0.67	3.02	0.45	0.00	15.03%	0.00%	84.97%
26	Argillaceous shale	4.58	0.09	5.23	56.89	16.83	0.00	0.63	2.99	0.30	0.00	10.01%	0.00%	89.99%
27	Mixed shale	5.95	0.07	2.06	57.38	16.73	0.00	0.65	3.03	0.24	0.00	7.80%	12.60%	79.60%
28	Argillaceous shale	5.18	0.05	2.18	58.52	17.24	0.00	0.66	3.00	0.31	0.00	10.19%	0.00%	89.81%
29	Mixed shale	5.80	0.05	3.57	57.37	16.10	0.40	0.64	3.15	0.29	0.04	9.30%	1.16%	89.54%
30	Argillaceous shale	5.83	0.19	7.42	51.46	14.30	0.59	0.59	3.18	0.42	0.07	13.25%	2.15%	84.60%
31	Argillaceous shale	5.26	0.12	4.07	55.18	16.22	0.00	0.63	3.01	0.47	0.00	15.52%	0.00%	84.48%
32	Argillaceous shale	5.20	0.13	5.34	54.10	15.40	0.02	0.62	3.10	0.39	0.00	12.56%	0.00%	87.44%
33	Argillaceous shale	5.63	0.04	4.28	56.63	15.73	0.66	0.63	3.18	0.40	0.07	12.54%	2.18%	85.28%
34	Argillaceous shale	5.22	0.06	1.72	60.09	16.68	0.72	0.67	3.18	0.40	0.07	12.43%	2.26%	85.31%
35	Argillaceous shale	5.62	0.04	3.13	57.34	16.64	0.00	0.64	3.04	0.37	0.00	12.31%	0.00%	87.69%
36	Mixed shale	4.52	0.06	4.20	49.44	13.85	0.39	0.63	3.15	0.36	0.04	11.50%	1.39%	87.12%
37	Mixed shale	5.80	0.03	0.79	59.30	17.69	0.00	0.66	2.96	0.45	0.00	15.05%	15.32%	69.63%
38	Argillaceous shale	5.67	0.07	1.28	58.63	17.40	0.00	0.66	2.98	0.44	0.00	14.63%	0.00%	85.37%
39	Argillaceous shale	6.33	0.07	3.38	57.18	16.02	0.44	0.64	3.15	0.45	0.04	14.16%	1.33%	84.50%

(*continued on next page*)

Table 3 (*continued*)

Sample name	Lithofacies	Major oxides (%)					Excess-Si	Si/(Si + Fe + Al + Ca)	(Si/Al)$_{total}$	(Si/Al)$_{S-I}$	(Si/Al)$_{Biogenic}$	SiO_2 illitization	SiO_2 biogenic	SiO_2 terrestrial
		Fe_2O_3	MnO	CaO	SiO_2	Al_2O_3								
40	Argillaceous shale	7.83	0.12	2.00	56.12	17.08	0.00	0.62	2.90	0.48	0.00	16.52%	0.00%	83.48%
41	Mixed shale	4.91	0.12	14.24	46.31	12.22	1.61	0.52	3.35	0.57	0.24	16.88%	7.12%	76.00%
42	Mixed shale	4.32	0.05	4.98	56.23	15.93	0.14	0.64	3.12	0.43	0.01	13.65%	5.01%	81.34%
43	Argillaceous shale	6.45	0.09	1.81	57.50	15.99	0.64	0.65	3.18	0.47	0.07	14.89%	2.08%	83.03%
44	Argillaceous shale	4.52	0.05	2.44	59.28	17.57	0.00	0.66	2.98	0.47	0.00	15.75%	0.00%	84.25%
45	Argillaceous shale	5.23	0.06	1.42	62.20	16.60	1.84	0.68	3.31	0.50	0.20	15.14%	6.02%	78.83%
46	Mixed shale	7.35	0.17	17.80	43.03	9.26	4.92	0.47	4.10	0.83	0.99	20.30%	24.21%	55.49%
47	Mixed shale	4.69	0.06	2.02	60.29	16.73	0.73	0.67	3.18	0.45	0.07	14.24%	2.29%	83.47%

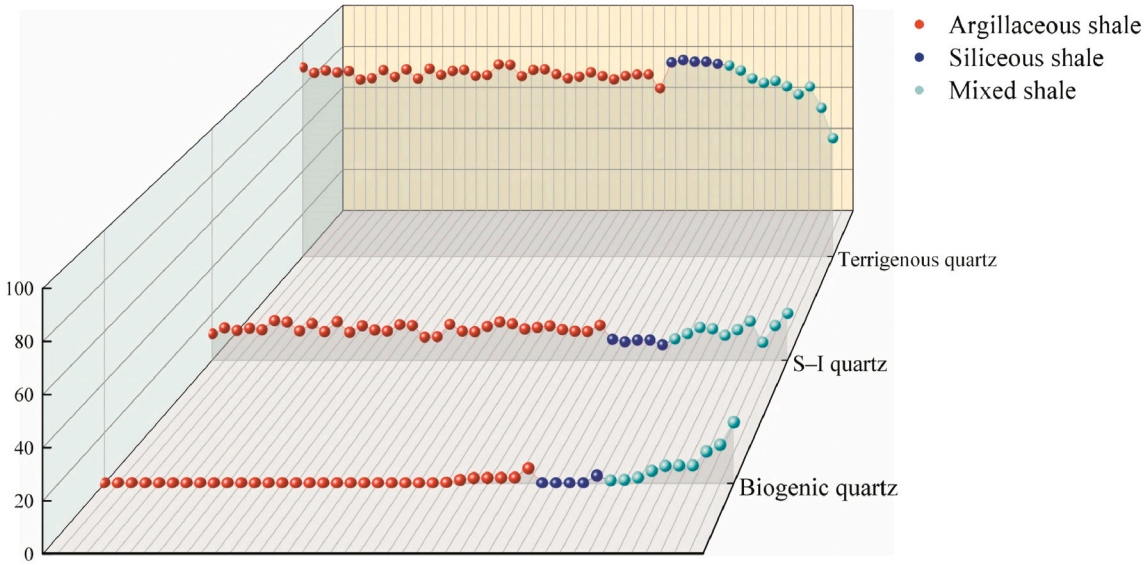

Fig. 12. Distribution of different types of quartz in the Qingshankou Formation shale.

and pore structure of the shale (Dong et al., 2019). These differences also influence the distribution and migration of different phase fluids, such as fluid connectivity and fkuid distribution within pores (Ge et al., 2020). Therefore, quartz origin is a crucial factor influencing the phase fluids. Because of the low content of biogenic quartz in the Qingshankou Formation shale (Table 3), the impacts of terrigenous clastic quartz and quartz formed by the smectite-to-illite transition on different phase fluids were analyzed.

5.3.1. *Multisource quartz and solid OM*

Solid OM includes kerogen, solid bitumen, heavy oil, and other high-viscosity hydrocarbon compounds with poor flowability. Owing to the limited instrument resolution, the accurate differnetiation of these components is challenging, and thus all components are classified as solid compounds. Their compositions make them the main contributors to the TOCs of the shale samples (Liu et al., 2019a). The quartz formed by the smectite-to-illite transition is not only the main source of authigenic quartz in the Qingshankou Formation shale in the southern

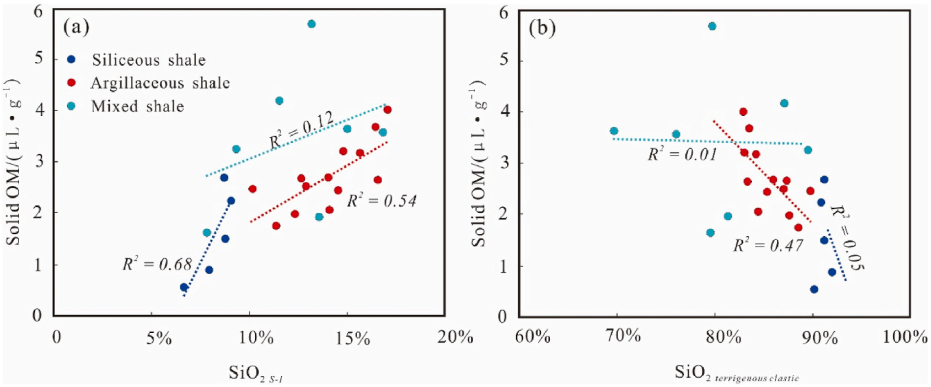

Fig. 13. Correlations between the contents of quartz of different origins and solid organic matter.

Songliao Basin but also the primary contributor to the solid OM in the shale. According to the cross plot of the quartz content transformed from the shale clay in the Qingshankou Formation in the southern Songliao Basin and solid OM, irrespective of whether it is in siliceous shale or clay shale, a linear positive correlation exists between the quartz content and solid OM (Fig. 13a). When the quartz source is terrigenous detrital quartz, a negative correlation exists between the quartz content and solid OM (Fig. 13b). Solid OM is affected by both the terrigenous detrital quartz outside the basin and authigenic quartz formed by the smectite-to-illite transition within the basin.

The presence of a high content of OM depends not only upon the production of significant biological OM but also on the mechanisms of OM preservation and resistance against oxidative degradation (Stow et al., 2001). The two primary factors contributing to the substantial presence of solid OM in the Qingshankou Formation shale are as follows.

(1) The conversion of the high clay mineral content into quartz plays a pivotal role in preserving solid OM. The depositional environment of the Qingshankou Formation is dominated by semideep to deep lakes, and the resulting quiet and anoxic environment is necessary for preserving a sufficient OM supply (Liu et al., 2019b). In areas lacking terrigenous felsic clasts, the stable hydrodynamic environment and low sedimentation rate lead to the accumulation of clay minerals at the lakebed, particularly at the center of the lake far from the source. This process results in a gradual increase in the clay mineral content in the shale. Authigenic quartz, formed by the smectite-to-illite transition, with its large specific surface area, readily adsorbs OM on the surface of clay mineral particles. Additionally, the illitization of montmorillonite can release fluids rich in free Si. The clay content in the Qingshankou Formation shale, which ranges from 32.0% to 69.1%, is primarily composed of illite and illite–smectite mixed layers (Table 1), indicating complete illitization. Free Si can migrate to adjacent reservoirs and precipitate and cement, becoming the main source of authigenic quartz in the reservoir. The transformation of clay minerals is widely known to concurrently occur with hydrocarbon generation due to the thermal evolution of OM (Metwally and Chesnokov, 2012). Consequently, authigenic quartz formed by the smectite-to-illite transition not only fills the primary matrix pores but also occupies a portion of the secondary organic pores, resulting in a positive correlation with a segment of the OM content in the Qingshankou Formation shale.

(2) Terrigenous detrital quartz diluted solid OM. During periods of sea level decline, an increase in the extra-basin (terrigenous) debris flux was observed to dilute the TOC in seafloor sediments, as in the Middle-Upper Devonian shales of the Appalachian Basin (Sageman et al., 2003). In the Qingshankou Formation shale, an inverse relationship is evident: as terrigenous quartz content increases, solid OM content decreases (Fig. 13b). This trend suggests that terrigenous detrital quartz fluxes diluted the concentration of OM. However, this dilution effect is more pronounced in argillaceous shale, primarily because the clay mineral content in argillaceous shale is significantly higher than in siliceous shale (Table 1), which enhances its ability to adsorb OM (Fig. 5). Consequently, the impact of terrigenous detrital quartz in diluting OM is more apparent in argillaceous shale.

5.3.2. *Multisource quartz and water*

During shale oil and gas accumulation, hydrocarbon-generating chemical reactions and diagenesis will discharge water, but some water will still remain inside shale pores bound to them (Li et al., 2019). The bound water occupies potential hydrocarbon space, hindering gas migration and directly affecting the enrichment and extraction of shale oil and gas. The statistical analysis of the relationship between the source of quartz and the content of water in its occurrence state reveals a association that the quartz formed by the smectite-to-illite transition is positively correlated to the water content (Fig. 14a), while the content of terrestrial detrital quartz is negatively correlated to the water content within the shale pores (Fig. 14b). Thus, the source of quartz occurring in argillaceous shale exerts a significant influence on shale water. The correlation between siliceous shale and mixed shale is weak (Fig. 14), which may be due to the inherent abundance of terrestrial detrital quartz particles in siliceous shale, known for their durability and resistance to chemical alterations. Conversely, the transformation of clay minerals within argillaceous shale into quartz could improve the connectivity of the shale pore structure, thereby enhancing water permeability of the shale. Moreover, the factors influencing water occurrence in shale are not limited to the type of quartz but also to shale pore type, size, specific surface area, and the degree of development.

6. Conclusions

This study focused on the shale reservoirs of the Lower Cretaceous Qingshankou Formation in the southern Songliao Basin in China. A comprehensive understanding of the types and origins of the quartz in

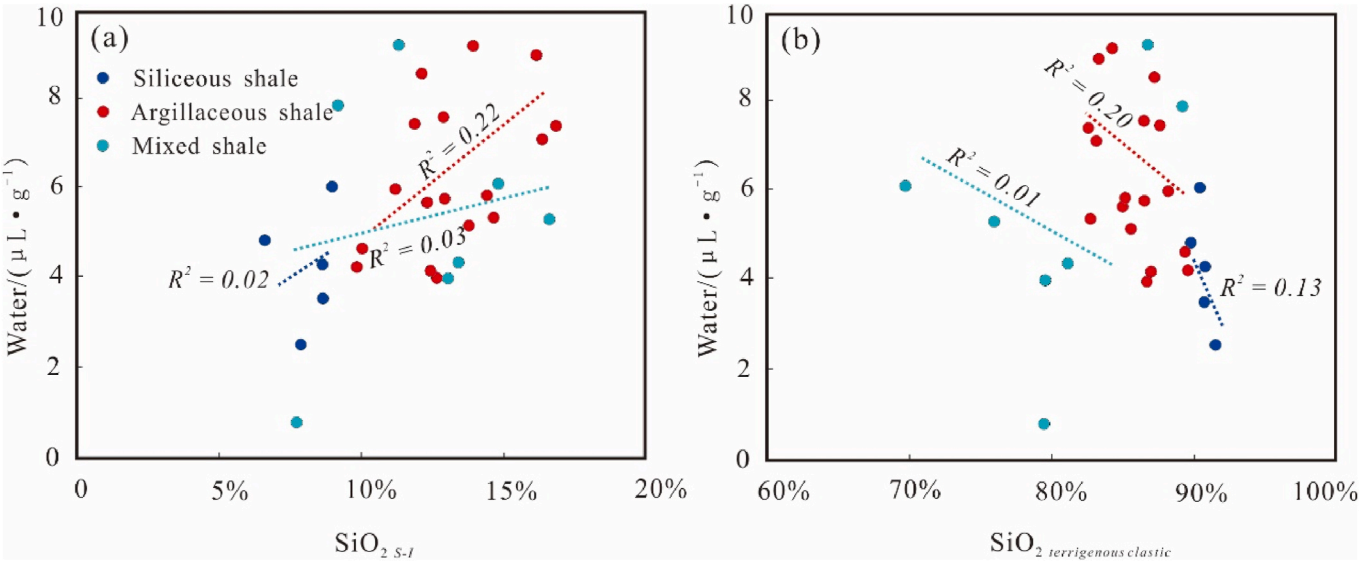

Fig. 14. Correlation between the contents of quartz of different origins and the content of water.

Qingshankou Formation shale was achieved employing various experimental techniques. Through this multifaceted approach, accurate identification and characterization of the different types of quartz in the Qingshankou Formation shale and their unique attributes were accomplished.

(1) The investigation successfully distinguished between detrital quartz and authigenic quartz in the Qingshankou Formation shale based on their petrographic characteristics, as revealed by the results of SEM and EDS analyses. Detrital quartz is characterized by silt-sized grains (5–20 μm) with surface traces of transportation and exhibits a pure SiO_2 composition. Alternatively, authigenic quartz with submicrometer-sized particles, some even reaching a few micrometers, is formed through silica precipitation occurring during the smectite-to-illite transition.
(2) The concentration of terrigenous clastic quartz ranges from 92.03% to 55.49%, with an average of 84.70%; the concentration of diagenetic quartz originating from the smectite-to-illite transition ranges from 20.30% to 6.67%, with an average of 13.12%, while the concentration of biogenic quartz ranges from 0% to 24.21%, with an average of 2.17%. These findings provide valuable insights into the distribution and abundance of quartz types within shale reservoirs.
(3) The solid OM and water contents vary among different lithofacies. Thus, lithofacies play a critical role in governing the sources of quartz, subsequently affecting the properties of the fluids in the shale reservoirs.

CRediT authorship contribution statement

Lei Li: Conceptualization, Investigation, Methodology, Software. **Zhidong Bao:** Conceptualization, Funding acquisition, Resources, Supervision, Writing – review & editing. **Zhongcheng Li:** Resources, Supervision. **Li Chen:** Methodology, Resources. **Xiaohong Xu:** Supervision, Validation. **Yilin Li:** Data curation, Software. **Yonggang Zhao:** Supervision, Writing – review & editing. **Xinmin Song:** Visualization, Writing – review & editing.

Declaration of competing interest

The authors declare that they have no known competing financial interests or personal relationships that could have appeared to influence the work reported in this paper.

Data availability

Data will be made available on request.

Acknowledgements

This work is jointly funded “the China Scholarship Council (No.202306440021), the National Key Research and Development Programs of China (Nos.2018YFC0604304, 2017YFC603104) “. The author would like to thank the staff members of Jilin Oilfield for providing the geological data. The authors would also like to thank the editors and for reviewers their time and efforts that have greatly improved the final manuscript.

References

Adachi, M., Yamamoto, K., Sugisaki, R., 1986. Hydrothermal chert and associated siliceous rocks from the northern Pacific their geological significance as indication od ocean ridge activity. Sediment. Geol. 47 (1–2), 125–148.
Bai, B., et al., 2022. Authigenic silica in continental lacustrine shale and its hydrocarbon significance. Petrol. Explor. Dev. 49 (5), 1033–1045.
Bai, L., Liu, B., Chi, Y., Li, S., Wen, X., 2021. D NMR studies of fluids in organic-rich shale from the Qingshankou Formation, Songliao Basin. Oil Gas Geol. 42 (6), 1389–1400.
Bechtel, A., et al., 2012. Palaeoenvironmental conditions during deposition of the Upper Cretaceous oil shale sequences in the Songliao Basin (NE China): implications from geochemical analysis. Org. Geochem. 46, 76–95.
Blattmann, T., et al., 2019. Mineralogical control on the fate of continentally derived organic matter in the ocean. Science 366 (6466), 742–745.
Boles, J.R., Franks, S.G., 1979. Clay diagenesis in Wilcox sandstones of Southwest Texas; implications of smectite diagenesis on sandstone cementation. J. Sediment. Res. 49 (1), 55–70.
Bowker, K.A., 2003. Recent developments of the barnett shale play. Fort Worth basin: West Texas Geological Society Bulletin 42 (6), 4–11.
Cao, T., Song, Z., Wang, S., Xia, J., 2016. Characterization of pore structure and fractal dimension of Paleozoic shales from the northeastern Sichuan Basin, China. J. Nat. Gas Sci. Eng. 35, 882–895.
Cavosie, A., Valley, J.W., Wilde, S.A., 2005. Magmatic δ18O in 4400–3900 Ma detrital zircons: a record of the alteration and recycling of crust in the Early Archean. Earth Planet Sci. Lett. 235 (3–4), 663–681.
Chen, X., et al., 2022. Origin of authigenic quartz in organic-rich shales of the Niutitang Formation in the northern margin of Sichuan Basin, South China: implications for pore network development. Mar. Petrol. Geol. 138.
D'Agostino, C., Mitchell, J., Mantle, M.D., Gladden, L.F., 2014. Interpretation of NMR relaxation as a tool for characterising the adsorption strength of liquids inside porous materials. Chem.–Eur. J. 20 (40), 13009–13015.
Dong, T., et al., 2021. Quartz types, origins and organic matter-hosted pore systems in the lower cambrian Niutitang Formation, middle yangtze platform, China. Mar. Petrol. Geol. 123.
Dong, T., et al., 2019. Quartz types and origins in the paleozoic Wufeng-Longmaxi Formations, Eastern Sichuan Basin, China: implications for porosity preservation in shale reservoirs. Mar. Petrol. Geol. 106, 62–73.
Dowey, P.J., Taylor, K.G., 2017. Extensive authigenic quartz overgrowths in the gas-bearing Haynesville-Bossier Shale, USA. Sediment. Geol. 356, 15–25.
Feng, Z., et al., 2010. Tectonostratigraphic units and stratigraphic sequences of the nonmarine Songliao basin, northeast China. Basin Res. 22 (1), 79–95.
Fleury, M., et al., 2013. Characterization and quantification of water in smectites with low-field NMR. J. Phys. Chem. C 117 (9), 4551–4560.
Fleury, M., Romero-Sarmiento, M., 2016. Characterization of shales using T1–T2 NMR maps. J. Petrol. Sci. Eng. 137, 55–62.
Gao, P., et al., 2022. Effect of silica diagenesis on porosity evolution of deep gas shale reservoir of the Lower Paleozoic Wufeng-Longmaxi formations, Sichuan Basin. Mar. Petrol. Geol. 145.
Garzanti, E., Andò, S., Vezzoli, G., 2008. Settling equivalence of detrital minerals and grain-size dependence of sediment composition. Earth Planet Sci. Lett. 273 (1–2), 138–151.
Ge, T., et al., 2020. Heterogeneity of pore structure of late Paleozoic transitional facies coal-bearing shale in the Southern North China and its main controlling factors. Mar. Petrol. Geol. 122, 104710.
Haq, B.U., 2014. Cretaceous eustasy revisited. Global Planet. Change 113, 44–58.
Jenkyns, H.C., 2010. Geochemistry of oceanic anoxic events. G-cubed 11 (3).
Josh, M., et al., 2012. Laboratory characterisation of shale properties. J. Petrol. Sci. Eng. 88, 107–124.
Langford, F., Blanc-Valleron, M.-M., 1990. Interpreting Rock-Eval pyrolysis data using graphs of pyrolizable hydrocarbons vs. total organic carbon. AAPG Bull. 74 (6), 799–804.
Lasemi, Z., Sandberg, P.A., Boardman, M.R., 1990. New microtextural criterion for differentiation of compaction and early cementation in fine-grained limestones. Geology 18 (4), 324–337.
Li, J., et al., 2019. Microdistribution and mobility of water in gas shale: a theoretical and experimental study. Mar. Petrol. Geol. 102, 496–507.
Liu, B., et al., 2019a. Geochemical characterization and quantitative evaluation of shale oil reservoir by two-dimensional nuclear magnetic resonance and quantitative grain fluorescence on extract: a case study from the Qingshankou Formation in Southern Songliao Basin, northeast China. Mar. Petrol. Geol. 109, 561–573.
Liu, B., et al., 2021. Reservoir space and enrichment model of shale oil in the first member of Cretaceous Qingshankou Formation in the Changling sag, southern Songliao Basin, NE China. Petrol. Explor. Dev. 48 (3), 608–624.
Liu, B., et al., 2019b. Lithofacies and depositional setting of a highly prospective lacustrine shale oil succession from the Upper Cretaceous Qingshankou Formation in the Gulong sag, northern Songliao Basin, northeast China. AAPG Bull. 103 (2), 405–432.
Loucks, R.G., Ruppel, S.C., 2007. Mississippian barnett shale: lithofacies and depositional setting of a deep-water shale-gas succession in the fort worth basin, Texas. AAPG (Am. Assoc. Pet. Geol.) Bull. 91 (4), 579–601.
MacLeod, K.G., Huber, B.T., Berrocoso, Á.J., Wendler, I., 2013. A stable and hot Turonian without glacial δ18O excursions is indicated by exquisitely preserved Tanzanian foraminifera. Geology 41 (10), 1083–1086.
Martínez, F., López, C., Parra, M., Espinoza, D., 2019. Testing the occurrence of thick-skinned triangle zones in the central andes forearc: example from the salar de Punta negra Basin in northern Chile. J. Struct. Geol. 120, 14–28.
Metwally, Y.M., Chesnokov, E.M., 2012. Clay mineral transformation as a major source for authigenic quartz in thermo-mature gas shale. Appl. Clay Sci. 55, 138–150.
Milliken, K.L., Esch, W.L., Reed, R.M., Zhang, T., 2012. Grain assemblages and strong diagenetic overprinting in siliceous mudrocks, barnett shale (mississippian), fort worth basin, TexasProperties of siliceous mudrocks, barnett shale, Texas. AAPG Bull. 96 (8), 1553–1578.
Milliken, K.L., Rudnicki, M., Awwiller, D.N., Zhang, T., 2013. Organic matter–hosted pore system, Marcellus formation (Devonian), Pennsylvania. AAPG Bull. 97 (2), 177–200.

Niu, X., et al., 2018. Origin of quartz in the lower cambrian niutitang Formation in south hubei province, upper yangtze platform. Mar. Petrol. Geol. 96, 271–287.
Pan, Z., Connell, L.D., 2015. Reservoir simulation of free and adsorbed gas production from shale. J. Nat. Gas Sci. Eng. 22, 359–370.
Peltonen, C., Marcussen, Ø., Bjørlykke, K., Jahren, J., 2009. Clay mineral diagenesis and quartz cementation in mudstones: the effects of smectite to illite reaction on rock properties. Mar. Petrol. Geol. 26 (6), 887–898.
Peng, J., Milliken, K.L., Fu, Q., Reid, C., 2020. Quartz types in the Upper Pennsylvanian organic-rich Cline Shale (Wolfcamp D), Midland Basin, Texas: implications for silica diagenesis, porosity evolution and rock mechanical properties. Sedimentology 67 (4), 2040–2064.
Rezente, B.H.J., 1988. Corg-reiche Sedimente Als Schlüssel Zum Verständnis Fossiler Schwarzschiefer. Göttingen University, Habilitation.
Ross, D.J., Bustin, R.M., 2009. Investigating the use of sedimentary geochemical proxies for paleoenvironment interpretation of thermally mature organic-rich strata: examples from the Devonian–Mississippian shales, Western Canadian Sedimentary Basin. Chem. Geol. 260 (1–2), 1–19.
Sageman, B.B., et al., 2003. A tale of shales: the relative roles of production, decomposition, and dilution in the accumulation of organic-rich strata, Middle–Upper Devonian, Appalachian basin. Chem. Geol. 195 (1–4), 229–273.
Sakuma, A., et al., 2022. Sedimentological and geochemical properties of authigenic carbonates in Kyushu, Japan: implications for the transition from semi-arid to humid climate during the Eocene. Sediment. Geol. 442.
Stow, D., Huc, A.-Y., Bertrand, P., 2001. Depositional processes of black shales in deep water. Mar. Petrol. Geol. 18 (4), 491–498.
Sun, L., et al., 2021. An analysis of major scientific problems and research paths of Gulong shale oil in Daqing Oilfield, NE China. Petrol. Explor. Dev. 48 (3), 527–540.
Tera, F., Wasserburg, G., 1972. U-Th-Pb systematics in three Apollo 14 basalts and the problem of initial Pb in lunar rocks. Earth Planet Sci. Lett. 14 (3), 281–304.
Van de Kamp, P.C., 2008. Smectite-illite-muscovite transformations, quartz dissolution, and silica release in shales. Clay Clay Miner. 56 (1), 66–81.
Wang, F., Feng, Z., Wang, X., Zeng, H., 2023. Effect of organic matter, thermal maturity and clay minerals on pore formation and evolution in the Gulong Shale, Songliao Basin, China. Geoenergy Science and Engineering 223, 211507.
Wang, L., et al., 2017. New permian-triassic conodont data from selong (tibet) and the youngest occurrence of vjalovognathus. J. Asian Earth Sci. 146, 152–167.
Wang, Y., et al., 2018. Characterization of organic matter pores in typical marine and terrestrial shales, China. J. Nat. Gas Sci. Eng. 49, 56–65.
Wedepohl, K., 1971. Environmental influences on the chemical composition of shales and clays. Phys. Chem. Earth 8, 307–333.
Williams, L.A., Parks, G.A., Crerar, D.A., 1985. Silica diagenesis; I, Solubility controls. J. Sediment. Res. 55 (3), 301–311.
Worden, R., Morad, S., 2000. Quartz cementation in oil field sandstones: a review of the key controversies. Quartz cementation in sandstones 1–20.
Xi, D., et al., 2016. Late Cretaceous marine fossils and seawater incursion events in the Songliao Basin, NE China. Cretac. Res. 62, 172–182.
Xi, Z., et al., 2019. Characterization of quartz in the Wufeng Formation in northwest Hunan Province, south China and its implications for reservoir quality. J. Petrol. Sci. Eng. 179, 979–996.
Xiong, Z., et al., 2022. Origin and significance of authigenic quartz and albite in lacustrine calcareous fine-grained sedimentary rocks. Mar. Petrol. Geol. 143.
Xu, H., et al., 2021. Quartz types, silica sources and their implications for porosity evolution and rock mechanics in the Paleozoic Longmaxi Formation shale, Sichuan Basin. Mar. Petrol. Geol. 128.
Yang, W., et al., 2018a. Effect of lithofacies on pore structure and new insights into pore-preserving mechanisms of the over-mature Qiongzhusi marine shales in Lower Cambrian of the southern Sichuan Basin, China. Mar. Petrol. Geol. 98, 746–762.
Yang, X., et al., 2018b. Different formation mechanism of quartz in siliceous and argillaceous shales: a case study of Longmaxi Formation in South China. Mar. Petrol. Geol. 94, 80–94.
Ye, Y., Tang, S., Xi, Z., Jiang, D., Duan, Y., 2022. Quartz types in the Wufeng-Longmaxi Formations in southern China: implications for porosity evolution and shale brittleness. Mar. Petrol. Geol. 137.
Yu, Y., Lin, L., Li, Z., Chen, H., 2022. Source of quartz cement in tight gas sandstone: evidence from the upper triassic xujiahe Formation in the western Sichuan Basin, SW China. J. Petrol. Sci. Eng. 212.
Zhang, L., Bao, Z., Dou, L., Xu, Q., 2021. Diagenetic alterations related to sedimentary architecture of deltaic distributary channels in red beds of the Cretaceous Yaojia Formation, Songliao Basin. J. Petrol. Sci. Eng. 203, 108564.
Zhang, P., et al., 2022. Lateral changes of organic matter preservation in the lacustrine Qingshankou Formation (Cretaceous Songliao Basin, NE China): evidence for basin segmentation. Int. J. Coal Geol. 254, 103984.
Zhang, Q., et al., 2019. Ediacaran, cambrian, ordovician, silurian and permian shales of the upper yangtze platform, south China: deposition, thermal maturity and shale gas potential. Int. J. Coal Geol. 216, 103281.
Zhang, Z., Cai, X., Zhang, M., Li, J., Zhang, Y., 2014. An analysis of the relationship between types of ostracoda shell ornaments and shell shapes and the environment from Late Cretaceous Qingshankou Formation to 1st Member of Nenjiang Formation in Songliao Basin. Chin. Geol. 41 (1), 135–147.
Zhou, Q., et al., 2022. Insight into the desorption behavior and mechanism of tight oil with in-situ low-temperature thermal. J. Petrol. Sci. Eng. 218, 111001.